Ultrasonics 94 (2019) 264–280

Contents lists available at ScienceDirect

Ultrasonics

journal homepage: www.elsevier.com/locate/ultras

Distributed point source modeling of the scattering of elastic waves by a circular cavity in an anisotropic half-space

Samaneh Fooladi[a,*], Tribikram Kundu[a,b]

[a] Department of Aerospace and Mechanical Engineering, University of Arizona, Tucson, AZ 85721, United States
[b] Department of Civil Engineering and Engineering Mechanics, University of Arizona, Tucson, AZ 85721, United States

ARTICLE INFO

Keywords:
DPSM
Ultrasonic waves
Greens function
Anisotropic material

ABSTRACT

The Distributed Point Source Method (DPSM) is a modeling technique based on superposition of fundamental solutions corresponding to individual pair of source and target points. A collection of source points distributed over the boundaries and interfaces are responsible for transmission, reflection, and refraction of acoustic waves in the solution domain. The strength of the source points may not be known a priory. By imposing the prescribed conditions on the boundaries and interfaces, a system of equations with the source strengths as the unknowns is obtained. After finding the source strengths as the solution to this system of equation, the amount of the solution at any target point in the domain is obtained by superimposing the effect of all source points on that target point. DPSM is an efficient modeling technique for ultrasonic problems since it does not require discretization of the whole solution domain but only the boundaries and interfaces. The fundamental solution, or the Green's function, between a pair of source and target points serves as the building block for DPSM. For an ideal fluid or a homogeneous isotropic solid the elastodynamic Green's function is available as closed form algebraic expressions. But for an anisotropic solids, the set of governing equations are considerably more complex and the elastodynamic Green's function needs to be evaluated numerically. In this study, an anisotropic half-space containing a flaw in the form of a circular hole is considered. The solid half-space is in contact with fluid and a transducer is located in fluid facing the solid half-space. Some efforts have been made to alleviate the computational intensity of the numerical evaluation of anisotropic Green's function for this problem. Firstly, a technique called "windowing" is used to exploit the repetitive pattern of relative positions of the source and target points in order to considerably reduce the number of Green's function evaluations. Secondly, the resolution of the integration for evaluation of the anisotropic Green's function is changed based on the distance between the source and target points, and a calibration technique based on an equivalent isotropic stiffness tensor is suggested. This calibrated multi-resolution integration technique is combined with the windowing technique, and the developed DPSM model is applied to a numerical example containing a transversely isotropic half-space, to show the applicability and effectiveness of DPSM modeling for this class of problems. Important applications like non-destructive evaluation of composite materials may benefit from such modeling capability.

1. Introduction

The Distributed Point Source Method (DPSM) is a modeling technique for computing a field in a solution domain based on superposition of fundamental solutions corresponding to individual pairs of points [1]. The collection of these individual points, referred to as source points, construct the boundaries and interfaces of the solution domain, and their collective effect on a point of interest, called target point, is obtained by superposition. DPSM does not need to discretize the whole problem geometry, but only needs to place sources along the interfaces and the boundaries. This strategy can be computationally very efficient for some applications, particularly when a localized feature in an otherwise large solution domain in 3D is of interest.

The DPSM can be used for modeling different types of physical problems involving mechanical, electrical, and magnetic fields. In particular, DPSM has been proven to be useful for modeling the traveling of acoustic waves in fluid and solid media [1,2]. This modeling capability is important for Non-Destructive Evaluation (NDE) of materials by ultrasound. In ultrasonic NDE [3], a mechanical pulse generated by a transducer travels into the material being examined, and if the material contains a flaw, then a portion of the pulse is scattered which can then be detected by a receiving transducer and sent to related

* Corresponding author.
E-mail address: sfooladi@email.arizona.edu (S. Fooladi).

https://doi.org/10.1016/j.ultras.2018.09.002
Received 26 April 2018; Received in revised form 4 September 2018; Accepted 5 September 2018
Available online 07 September 2018
0041-624X/

electrical equipment for analyzing. A pulse generated by a transducer can be considered as a superposition of harmonic waves, where in most cases the significant frequency components range roughly from 50 kHz to 20 MHz. In analyzing the response of the NDE system, the response functions of individual parts contribute to the overall response of the system via multiple convolution integrals. These integrals are however convertible to simple products of response functions, if one takes their Fourier transform and works in frequency domain instead of the time domain. Computational acoustic models may be required to obtain the response functions for propagation and scattering of harmonic waves in fluid and solid in 3D.

A variety of methods are available for modeling wave propagation in fluid and solid. Finite Difference Method (FDM) [4,5] and Finite Element Method (FEM) [6,7] are among the well-established methods which work by discretizing the differential equations over the volume of the solution domain. As another domain-based method, Finite Integration Technique (FIT) [8] can be mentioned which starts from integral form of governing equations. FIT was initially developed in electromagnetics [9], and later adopted in elastodynamics [10,11]. The other class of methods applicable to wave propagation problems discretize the boundary instead of the volume of the solution domain. The most well-known method in this category is probably the Boundary Element Method (BEM) [12,13]. Among the methods more specialized to wave propagation problems are Gaussian beam models [14,15] and Distributed Point Source Method (DPSM) [1,2]. Also, one may concentrate on discretization of the wave front via the ray tracing method [16]. Another important modeling technique is Local Interaction Simulation Approach (LISA) [17,18] which is combined with FEM in [19] for modeling damped guided wave in composite structures.

BEM can be used for modeling elastic wave propagation problems. BEM starts from the boundary integral equation for elastodynamics which relates the displacement within the volume to displacement and traction over the boundary [20]. A collection of elements over the boundary are then responsible for discretizing the governing equations. Excellent reviews on BEM are given in [20,12,13].

Approximating via Gaussian beams is another way of modeling wave propagation problems. Ultrasound transducers generate highly directional beams which can be approximated as a superposition of Gaussian beams satisfying paraxial wave equation [3]. One can also consider pulses of finite length in the form of harmonically modulated Gaussian envelopes, in contrast to Gaussian beams which exhibit infinite length. Norris [14] studied the propagation of such finite pulses for anisotropic elastic solids. Roberts [21] modeled transmission of ultrasonic beams from an isotropic to transversely isotropic half-space as an angular spectrum of plane waves. Newberry and Thompson [22] utilized a Fresnel approximation to formulate an angular spectrum of plane waves in anisotropic solids.

Another method for modeling wave propagation problems is FEM [6,7]. FEM is a well-established method for numerical modeling of engineering problems [23]. A version of FEM called Spectral Element Method (SEM) has particularly gained attention for wave propagation modeling [24,25]. In SEM, different types of basis function, including Fourier series, Chebyshev polynomials, and Legendre polynomials, can be used in accordance with the requirements of the problem [26]. Polynomial-based SEM with proper choice of integration points may lead to a diagonal mass matrix which is able to benefit from the convenience of a fully explicit solver [27]. SEM has been used for wave propagation in anisotropic media [28,26,29]. SEM generally provides higher accuracy and better structured matrices in comparison to standard FEM, but it is more difficult to program, and also inherits some drawbacks of spectral methods, including more computational cost per degree of freedom and heavier loss on irregular grids [26]. Other advanced variants of FEM have also been considered for wave propagation problems in anisotropic media [30], and efforts have been made to reduce the computational burden of FEM [31].

FEM offers several advantages for modeling structural problems. It is versatile in terms of constitutive law, available via commercial softwares, and well-studied in different parts. But, FEM is a domain-based method which requires discretizing the volume of the geometry. In ultrasonic problems, one is usually interested in linear small-deformation waves scattered by local features like cracks and inclusions in an otherwise large domain in 3D, where the waves may propagate far away from the localized feature. The FEM modeling of such problems requires meshing a large 3D domain and the use of absorbing boundaries. Discretizing a 3D domain may become computationally prohibitive, and the reflection of waves from absorbing boundaries may not be totally avoided.

In the beginning of the 21st century, Distributed Point Source Method (DPSM) was developed for solving electrostatic, electromagnetic and ultrasonic wave propagation problems [32,33,2]. Later DPSM was extended to solve other problems such as high frequency fluid flow machinery problems [34] and fluid mechanics problems involving flow around an obstacle [35].

The Distributed Point Source Method (DPSM) is a collocation-type semi-analytical method which discretizes the solution domain over the boundary. Therefore, DPSM analyzes a 3D domain via its 2D boundary which results in a considerable reduction in size of the problem. DPSM is also well-suited for modeling local features in infinite domains since it does not need absorbing boundaries and does not suffer from numerical dispersion within the volume. However, in contrast to FEM which connects a chain of overlapping patches of interpolating functions, DPSM superimposes a series of fundamental solutions where each of them affects the whole volume and interacts with possibly all other fundamental solutions. Therefore, DPSM generally produces a dense global matrix with relatively large condition number, in comparison to the well-conditioned sparse matrix of classical FEM. Therefore, solving the system of equations may be more demanding for DPSM per degree of freedom, and requires more attention to the type of solver and the management of round-off errors. Nevertheless, DPSM has demonstrated superior performance in comparison to FEM in terms of saving computational time, particularly for modeling ultrasonic and electromagnetic wave propagation problems[2,34,36,37]. For example, a three-dimensional (3D) wave field modeling in a homogeneous fluid in front of a square transducer could be solved by DPSM order of magnitudes faster than COMSOL Multi-Physics FEM code on the same computer [2]. Jarvis and Cegla [36] compared DPSM and FEM for solving ultrasonic wave reflection from a rough surface and concluded, *“[FEM solution is] two orders of magnitude slower than the equivalent DPSM simulation on the same machine.”*

In spite of having this huge advantage in computational speed for DPSM, its use has been mostly limited to homogeneous and non-homogeneous media where every material in the problem geometry is isotropic. Only recently, Fooladi and Kundu [38] extended DPSM technique to an anisotropic solid containing no defect. Their technique is extended further in this paper to model scattering of ultrasonic waves in a defective anisotropic solid. Adding the defect is an important and necessary step toward making this technique applicable to simulation of NDE experiment. Also, a technique called “windowing” has been extended in this work for the case when a regular pattern is partially disturbed by an abnormality. In addition, a method for automatic calibration of multi-resolution integration technique has been proposed and developed in this paper.

In NDE applications, it is common to immerse a solid sample in a fluid, and place a transducer in the fluid facing the solid. The transducer generates ultrasonic pulses which travel through the fluid and then penetrates into the solid. The received pulses are then analysed to detect the existence of flaws inside the solid. In this study, DPSM is used to model the propagation of harmonic waves in an anisotropic solid exhibiting different mechanical stiffness in different directions and containing a defect. Anisotropic Materials, such as composites, have nowadays found important applications in various fields, and are heavily being used in industry.

As mentioned before, DPSM makes use of the fundamental solution between a pair of source and target points as its building block to construct the computational model. The fundamental solution, called the elastodynamic Green's function, is available as closed form expression, for some media like ideal fluids and isotropic solids. But, adding anisotropy to the problem results in a considerably more complex set of equations for which a closed form solution for the Green's function seems to be beyond reach. The Green's function needs to be evaluated numerically in this scenario, which may increase both mathematical complexity and computational intensity of the DPSM model.

The problem of wave propagation in a homogeneous isotropic half-space being in contact with fluid has been modeled by DPSM [39]. The same problem but with plate instead of half-space has been also studied [40]. A finite-size scatterer can be added to this problem by treating the scatterer surface as an internal interface and placing a collection of point sources along it [41]. The scatterer can be representative of a flaw such as a crack, cavity, or inclusion. In [42], the problem of a cylindrical hole in an isotropic half-space was considered, whereas the problem of an elliptical cavity in an isotropic half-space was considered [43]. By increasing the ratio of the principal axes of the ellipse (major/minor), the traction-free surface of a crack can be modeled. The interface between fluid and solid is assumed to be planar resembling the immersion of a planar solid plate in fluid. But, the application of DPSM is not limited to planar interfaces and the placement of the source points on the interface is not restricted by the interface curvature. Non-planar and relatively complex geometries for solid-fluid interface have been also studied by DPSM [44–46]. In all of the above studies the solid is assumed to be homogeneous and isotropic. The application of DPSM for ultrasound modeling was later extended to anisotropic solid plates immersed in fluid by Fooladi and Kundu [38]. Here, in continuation of that work, an anisotropic half-space containing a cylindrical hole and in contact with fluid is considered, and the resulting DPSM model is studied.

As mentioned previously, the elastodynamic Green's function should be evaluated numerically for anisotropic solid. The formulation developed by Wang and Achenbach[47] for computation of elastodynamic time-harmonic Green's functions for anisotropic solids is adopted here. The governing equations are in the form of a system of coupled PDEs which are reduced to ODEs by applying the Radon transform. Then, the coordinates are rotated in order to uncouple the ODEs. After finding the solution of the governing equations in the transformed rotated state, they are rotated back, and inverse Radon transform is applied to bring them back to the spatial coordinates. During this transformation process, two integrals are generated; one of them contains singular terms and is in the form of a 1D integral over an inclined circle on a unit sphere, while the other one contains non-singular terms and is in the form of a 2D integral over the surface of a hemi-sphere.

The non-singular or regular part, being in the form of a 2D integral, is responsible for the lion share of the computational time in evaluating the elastodynamic Green's function for anisotropic solids. In this regard, any effort in reducing its computational cost may have a tangible effect on computational adequacy of the whole DPSM model. Composites with transversely isotropic structure can be understood as one of the main classes of anisotropic materials which have extensive industrial applications. For these materials, the integration domain of the regular part can be reduced from a hemi-sphere to a quarter sphere, as was shown by Fooladi and Kundu [48,38]. The same technique is used here. In addition, a technique called "windowing" was suggested in [38] which made use of the regular pattern of relative positions of the source and target points in order to avoid repetitive evaluation of the Green's function. This technique is very effective in reducing the number of evaluations of the Green's function, and is extended here to the case of a domain with a hole for which only a portion of the domain remains regular. As another attempt to further reduce the computational cost, a calibration strategy is suggested here to optimize the number of integration points for the regular part of the Green's function in terms of the distance between the source and target points. This calibration is based on an equivalent isotropic stiffness tensor, and results in a multi-resolution integration technique which sets automatically an optimum number of integration points for a finite number of distance intervals between the source and target points.

The remainder of this paper is organized in the following manner. In Section 2, the DPSM model of an anisotropic half-space containing a hole and in contact with fluid is presented. In Section 3, the windowing technique is described. In Section 4 the elastodynamic Green's function for an ideal fluid, and in Section 5 the elastodynamic Green's function for an anisotropic solid are addressed. In Section 6, the multi-resolution calibration technique is formulated. In Section 7, the numerical results for a sample problem containing transversely isotropic half-space are presented. Lastly, in Section 8 the conclusion is given.

2. DPSM for a solid half-space containing a hole

In this section the formulation of DPSM for a solid half-space containing a hole and being in contact with a fluid half-space at its boundary will be presented. The formulation of DPSM for this configuration has been considered in [1,41].

The problem configuration is schematically shown in Fig. 1. In this figure, a solid half-space containing a cylindrical hole is located at the top, and is in contact with the fluid half-space which is located at the bottom. A flat circular transducer is placed inside the fluid at an inclination with respect to the horizontal plane (x_1–x_2 plane). The transducer generates the ultrasonic wave, and the fluid transmits the wave to the solid half-space where the wave is scattered by the hole.

In DPSM, a collection of source points generate the ultrasonic field at the target points. In other words, the Green's function of source points is computed at the location of the target points. To formulate the DPSM problem, we start by defining the sets of target points and then the source points. Three sets of target points are shown in Fig. 1: the set R_T which represents the points on the transducer surface, the set R_I which represents the points distributed over the fluid-solid interface, and the set R_H which represents the points distributed over the surface of the hole. These 3 sets of target points are listed in Table 1.

Next, the source points will be defined. The target points, defined

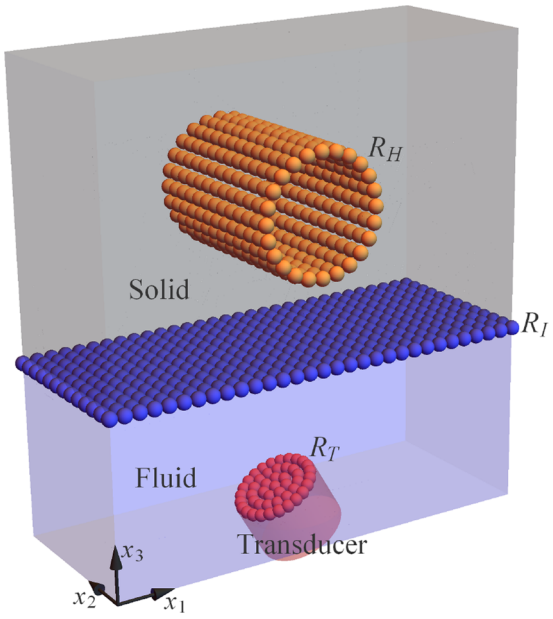

Fig. 1. Problem configuration: the target points R_T are located on the surface of transducer, the target points R_I are located on the interface between fluid and solid, and the target points R_H are located on the surface of the hole.

Table 1
Sets of target points.

Set	Location
R_T	Located on the surface of transducer
R_I	Located on the interface between fluid and solid
R_H	Located on the surface of the hole

previously, were placed exactly on the transducer surface, fluid-solid interface, and hole surface. But for the source points, placing them at such locations generates singularity due to $1/r$ term in the Green's function. Therefore, in order to avoid the singularity, the location of the source points is shifted from the location of the target points by a small value δ. This small value is equal to the radius of the spheres assigned to the points. In other words, a source point will be in contact with its corresponding surface (e.g. transducer surface, fluid-solid interface, or hole surface) via a sphere of radius δ whose center is at the source point.

The radius δ is obtained by requiring that the area of the hemisphere around the source point be equal to the corresponding area on the surface which is represented by the source point. Therefore, if a surface with total area S is represented by a collection of n source points, then each source point represents an area of S/n and the radius δ is [1]

$$\delta = \sqrt{\frac{1}{2\pi}\frac{S}{n}} \tag{1}$$

By increasing the resolution of the DPSM model, the number n increases in the above equation and the radius δ decreases. This means the location of the source points becomes closer to the location of target points when the resolution is increased, and the two sets coincide when n goes to infinity.

From the three sets of target points for this problem, and the value of the parameter δ, four sets of source points are defined which are listed in Table 2. The set $R_T^{-\delta}$ contains active source points representing the direct effect of the transducer on the fluid. The set R_I^{δ} contains passive source points representing the effect of reflected waves from solid to the fluid. The set $R_I^{-\delta}$ contains passive source points representing the effect of transmitted waves from the fluid to the solid. Finally, the set $R_H^{-\delta}$ contains the passive source points representing the scattered field due to the traction-free surface of the hole.

The locations of source and target points are shown in Fig. 2 where the three sets of target points R_T, R_H, and R_I are shown in Fig. 2(a), while the four sets of source points $R_T^{-\delta}$, R_I^{δ}, $R_I^{-\delta}$, and $R_H^{-\delta}$ are shown in Fig. 2(b).

A scalar source strength $A_f(\boldsymbol{x})$ is assigned to each source point $\boldsymbol{x}$ located in the fluid. This source strength is proportional to the pressure at that point. To be more specific, assume the Green's function for pressure in the fluid is given by $G_f^p(\boldsymbol{x}, \boldsymbol{y})$ where the subscript f represents fluid, the superscript p represents the pressure, and the vectors $\boldsymbol{x}$ and $\boldsymbol{y}$ represent the locations of source and target points in the Green's function, respectively. Then, the amount of pressure at the target point $\boldsymbol{y}$ due to a source of strength $A_f(\boldsymbol{x})$ at point $\boldsymbol{x}$ with a source strength $A_f(\boldsymbol{x})$ is equal to $A_f(\boldsymbol{x})G_f^p(\boldsymbol{x}, \boldsymbol{y})$. Other quantities like displacement and velocity are also proportional to source strength $A_f(\boldsymbol{x})$ in linear problems.

Table 2
Sets of source points.

Set	Location
$R_T^{-\delta}$	Shifted from R_T by $x_3 = -\delta$
$R_I^{-\delta}$	Shifted from R_I by $x_3 = -\delta$
R_I^{δ}	Shifted from R_I by $x_3 = \delta$
$R_H^{-\delta}$	Shifted from R_H by $-\delta$ along the radial direction

Now from the linearity assumption, the solution at an arbitrary target point in the fluid can be obtained by superposition of the influence of all individual source points affecting the fluid. A target point in the fluid is affected by the source points in sets $R_T^{-\delta}$ and R_I^{δ}, as is shown schematically in Fig. 3.

Let us define the new set R_f as

$$R_f = R_T^{-\delta} \cup R_I^{\delta} \tag{2}$$

where the subscript f refers to the fluid, and $\cup$ is the union symbol. The source points in R_f are responsible for the solution at any point in the fluid.

Assume that we are interested in a quantity $q(\boldsymbol{x})$ at location $\boldsymbol{x}$ in the fluid. This quantity can be pressure, displacement, velocity, etc. This quantity can be obtained by superimposing the effect of all the source points in R_f on the target point $\boldsymbol{x}$ as

$$q(\boldsymbol{x}) = \sum_{\boldsymbol{y}\in R_f} G_f^q(\boldsymbol{x}, \boldsymbol{y}) A_f(\boldsymbol{y}) \tag{3}$$

where G_q^f refers to the Green's function of the quantity q in the fluid denoted by f. The above relation can be rewritten in vector form as

$$q(\boldsymbol{x}) = \boldsymbol{M}_f^q(\boldsymbol{x}) \cdot \boldsymbol{A}_f \tag{4}$$

where

$$\boldsymbol{M}_f^q(\boldsymbol{x}) = \{G_f^q(\boldsymbol{x}, \boldsymbol{y}), \boldsymbol{y} \in R_f\} \tag{5}$$

$$\boldsymbol{A}_f = \{A_f(\boldsymbol{y}), \boldsymbol{y} \in R_f\} \tag{6}$$

and the vectors $\boldsymbol{M}_f^q(\boldsymbol{x})$ and $\boldsymbol{A}_f$ have the same size as R_f.

If there are n points in the set R_f shown by $\boldsymbol{y}_1$, $\boldsymbol{y}_2$, ..., $\boldsymbol{y}_n$, then the vectors $\boldsymbol{M}_f^q(\boldsymbol{x})$ and $\boldsymbol{A}_f$ can be written in expanded form as

$$\boldsymbol{M}_f^q(\boldsymbol{x}) = \{G_f^q(\boldsymbol{x}, \boldsymbol{y}_1),\ G_f^q(\boldsymbol{x}, \boldsymbol{y}_2), ...,\ G_f^q(\boldsymbol{x}, \boldsymbol{y}_n)\} \tag{7}$$

$$\boldsymbol{A}_f = \{A_f(\boldsymbol{y}_1),\ A_f(\boldsymbol{y}_2), ...,\ A_f(\boldsymbol{y}_n)\} \tag{8}$$

The vector $\boldsymbol{M}_f^q(\boldsymbol{x})$ will be later used to assemble the global system of equations from which the source strengths are obtained.

The attention is now turned to the solid and a procedure similar to that of fluid is followed in this case. For the solid, a vector of source strength $\boldsymbol{A}_s(\boldsymbol{x})$ with 3 components is assigned to each source point $\boldsymbol{x}$ where those 3 components correspond to the 3 components of a force vector in an orthonormal basis of 3D space. An arbitrary target point in the solid is affected by the source points in $R_I^{-\delta}$ and R_H^{δ}, as shown schematically in Fig. 4.

The new set R_s is defined as

$$R_s = R_I^{-\delta} \cup R_H^{\delta} \tag{9}$$

Then, a quantity $q(\boldsymbol{x})$ at point $\boldsymbol{x}$ in the solid can be obtained as

$$q(\boldsymbol{x}) = \sum_{\boldsymbol{y}\in R_s} \boldsymbol{G}_s^q(\boldsymbol{x}, \boldsymbol{y}) \cdot \boldsymbol{A}_s(\boldsymbol{y}) \tag{10}$$

where the vector $\boldsymbol{G}_q^s$ refers to the Green's function of the quantity q in the solid denoted by s. Note that for a scalar quantity q there are 3 components for the vector of the Green's function $\boldsymbol{G}_q^s$ and also the vector of the source strength $\boldsymbol{A}_s$. These vectors can be written in expanded form as

$$\boldsymbol{G}_s^q(\boldsymbol{x}, \boldsymbol{y}) = \{G_{s1}^q(\boldsymbol{x}, \boldsymbol{y}),\ G_{s2}^q(\boldsymbol{x}, \boldsymbol{y}),\ G_{s3}^q(\boldsymbol{x}, \boldsymbol{y})\} \tag{11}$$

$$\boldsymbol{A}_s(\boldsymbol{y}) = \{A_{s1}(\boldsymbol{y}),\ A_{s2}(\boldsymbol{y}),\ A_{s3}(\boldsymbol{y})\} \tag{12}$$

where the subscripts 1, 2, and 3 correspond to the 3 main directions in an orthonormal coordinate system in 3D space.

Eq. (10) can be rewritten as

$$q(\boldsymbol{x}) = \boldsymbol{M}_s^q(\boldsymbol{x}) \cdot \boldsymbol{A}_s \tag{13}$$

where

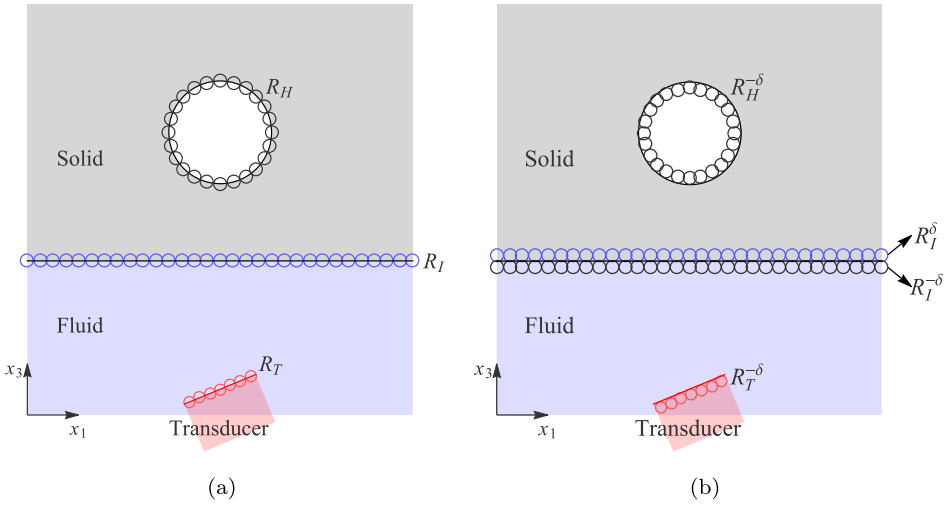

Fig. 2. Problem configuration: (a) target points, (b) source points.

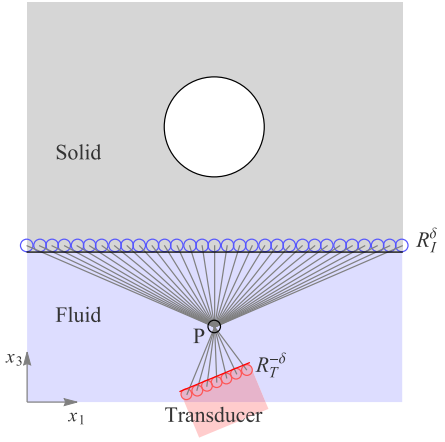

Fig. 3. A point P in fluid is affected by the source points in sets $R_T^{-\delta}$ and R_I^{δ}.

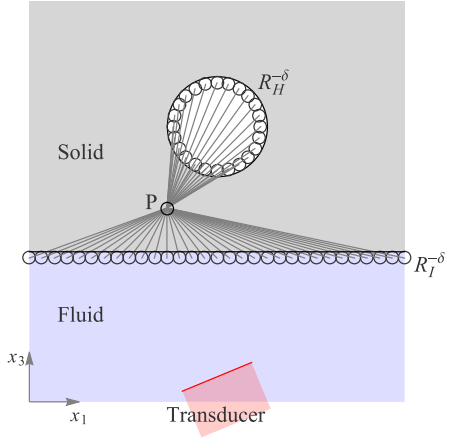

Fig. 4. A point P in the solid is affected by the source points in sets $R_I^{-\delta}$ and $R_H^{-\delta}$.

$$\boldsymbol{M}_s^q(\boldsymbol{x}) = \{\boldsymbol{G}_s^q(\boldsymbol{x}, \boldsymbol{y}), \boldsymbol{y} \in R_s\} \tag{14}$$

$$\boldsymbol{A}_s = \{\boldsymbol{A}_s(\boldsymbol{y}), \boldsymbol{y} \in R_s\} \tag{15}$$

and the vectors $\boldsymbol{M}_s^q(\boldsymbol{x})$ and $\boldsymbol{A}_s$ have $3n$ components where $n = \text{size}(R_s)$.

If there are n points in the set R_s denoted by $\boldsymbol{y}_1$, $\boldsymbol{y}_2$, ..., $\boldsymbol{y}_n$, then the vectors $\boldsymbol{M}_s^q(\boldsymbol{x})$ and $\boldsymbol{A}_s$ can be written in expanded form as

$$\begin{aligned}\boldsymbol{M}_s^q(\boldsymbol{x}) = \{&G_{s1}^q(\boldsymbol{x}, \boldsymbol{y}_1),\ G_{s2}^q(\boldsymbol{x}, \boldsymbol{y}_1),\ G_{s3}^q(\boldsymbol{x}, \boldsymbol{y}_1),\\ &G_{s1}^q(\boldsymbol{x}, \boldsymbol{y}_2),\ G_{s2}^q(\boldsymbol{x}, \boldsymbol{y}_2),\ G_{s3}^q(\boldsymbol{x}, \boldsymbol{y}_2), ...,\\ &G_{s1}^q(\boldsymbol{x}, \boldsymbol{y}_n),\ G_{s2}^q(\boldsymbol{x}, \boldsymbol{y}_n),\ G_{s3}^q(\boldsymbol{x}, \boldsymbol{y}_n)\}\end{aligned} \tag{16}$$

and

$$\begin{aligned}\boldsymbol{A}_s = \{&A_{s1}(\boldsymbol{y}_1),\ A_{s2}(\boldsymbol{y}_1),\ A_{s3}(\boldsymbol{y}_1),\\ &A_{s1}(\boldsymbol{y}_2),\ A_{s2}(\boldsymbol{y}_2),\ A_{s3}(\boldsymbol{y}_2), ...,\\ &A_{s1}(\boldsymbol{y}_n),\ A_{s2}(\boldsymbol{y}_n),\ A_{s3}(\boldsymbol{y}_n)\}\end{aligned} \tag{17}$$

respectively. The vector $\boldsymbol{M}_s^q(\boldsymbol{x})$ will be later used to assemble the global system of equations from which the source strengths are obtained.

Now, the boundary and interface conditions are defined and applied based on Eqs. (4) and (13). They construct a system of equations whose solution gives the amount of source strength for the source points in fluid and solid. Let us denote the source strength by $\boldsymbol{A}_f$ for the set R_f, and by $\boldsymbol{A}_s$ for the set R_s.

The first condition is related to the surface of the transducer. We assume the transducer vibrates with a constant velocity amplitude v_0. Therefore, for any point in the fluid adjacent to the transducer surface the normal velocity is equal to v_0. This condition can be written as

$$v_n(\boldsymbol{x}) = v_0, \quad \boldsymbol{x} \in R_T \tag{18}$$

Using Eq. (4), the above condition can be written as

$$\boldsymbol{M}_f^v(\boldsymbol{x}) \cdot \boldsymbol{A}_f = v_0, \quad \boldsymbol{x} \in R_T \tag{19}$$

The fluid is assumed to be non-viscous. Therefore, there is no constraint on the components of the velocity which are tangential to the transducer surface.

Next, the conditions at the fluid-solid interface are considered. At the interface, the normal displacement and the normal stress are continuous, and the shear stress is zero due to the assumption of having non-viscous fluid. The continuity of the displacement at the interface can be written as

$$u_3(\boldsymbol{x})|_{\text{in fluid}} = u_3(\boldsymbol{x})|_{\text{in solid}}, \quad \boldsymbol{x} \in R_I \tag{20}$$

Using Eq. (4) for fluid and Eq. (13) for solid, the above relation can be written as

$$\boldsymbol{M}_f^{u_3}(\boldsymbol{x}) \cdot \boldsymbol{A}_f - \boldsymbol{M}_s^{u_3}(\boldsymbol{x}) \cdot \boldsymbol{A}_s = 0, \quad \boldsymbol{x} \in R_I \tag{21}$$

The continuity of normal stress at the interface can be written as

$$-p(\boldsymbol{x})|_{\text{in fluid}} = \sigma_{33}(\boldsymbol{x})|_{\text{in solid}}, \quad \boldsymbol{x} \in R_I \tag{22}$$

Using Eq. (4) for fluid and Eq. (13) for solid, the above relation can be written as

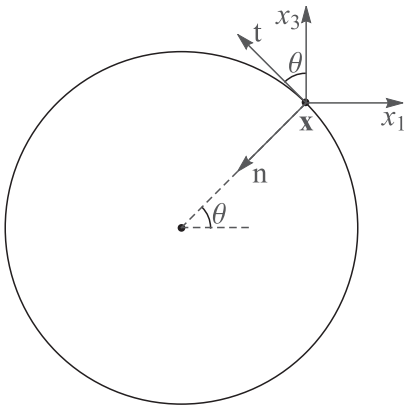

Fig. 5. The local coordinate system constructed at point $\boldsymbol{x}$.

$$\boldsymbol{M}_f^{p}(\boldsymbol{x})\cdot\boldsymbol{A}_f + \boldsymbol{M}_s^{\sigma_{33}}(\boldsymbol{x})\cdot\boldsymbol{A}_s = 0, \quad \boldsymbol{x}\in R_I \tag{23}$$

The shear stress is zero at the interface due to non-viscosity.

$$\sigma_{23}(\boldsymbol{x}) = 0, \quad \boldsymbol{x}\in R_I \tag{24}$$

$$\sigma_{31}(\boldsymbol{x}) = 0, \quad \boldsymbol{x}\in R_I \tag{25}$$

Using Eq. (13), the above relations can be written as

$$\boldsymbol{M}_s^{\sigma_{23}}(\boldsymbol{x})\cdot\boldsymbol{A}_s = 0, \quad \boldsymbol{x}\in R_I \tag{26}$$

$$\boldsymbol{M}_s^{\sigma_{31}}(\boldsymbol{x})\cdot\boldsymbol{A}_s = 0, \quad \boldsymbol{x}\in R_I \tag{27}$$

Next, the traction-free condition on the hole surface is considered. At each point $\boldsymbol{x}$ a local coordinate system on the hole surface is constructed as shown in Fig. 5. This local coordinate system consists of n being the normal to the hole surface, t being the tangent to the hole surface in x_1x_3 plane, and x_2 being the other tangential direction. The traction-free condition on the hole surface can be written in this local coordinate system as

$$\sigma_{nn}(\boldsymbol{x}) = 0, \quad \boldsymbol{x}\in R_H \tag{28}$$

$$\sigma_{x_2n}(\boldsymbol{x}) = 0, \quad \boldsymbol{x}\in R_H \tag{29}$$

$$\sigma_{nt}(\boldsymbol{x}) = 0, \quad \boldsymbol{x}\in R_H \tag{30}$$

Using Eq. (13), the above relations can be written as

$$\boldsymbol{M}_s^{\sigma_{nn}}(\boldsymbol{x})\cdot\boldsymbol{A}_s = 0, \quad \boldsymbol{x}\in R_H \tag{31}$$

$$\boldsymbol{M}_s^{\sigma_{x_2n}}(\boldsymbol{x})\cdot\boldsymbol{A}_s = 0, \quad \boldsymbol{x}\in R_H \tag{32}$$

$$\boldsymbol{M}_s^{\sigma_{nt}}(\boldsymbol{x})\cdot\boldsymbol{A}_s = 0, \quad \boldsymbol{x}\in R_H \tag{33}$$

The stress tensor in the rotated coordinate system can be obtained as

$$[\boldsymbol{\sigma}]^{tx_2n} = [\boldsymbol{Q}]^T\cdot[\boldsymbol{\sigma}]^{x_1x_2x_3}\cdot[\boldsymbol{Q}] \tag{34}$$

where $[\boldsymbol{Q}]$ is the rotation matrix.

$$[\boldsymbol{Q}] = \begin{bmatrix} \cos\theta & 0 & -\sin\theta \\ 0 & 1 & 0 \\ \sin\theta & 0 & \cos\theta \end{bmatrix} \tag{35}$$

Simultaneous solution of Eqs. (19), (21), (23), (26), (27), (31), (32), and (33) gives the values of source strengths at all source points in the fluid and in the solid.

To construct the global system of equations, let us define the following notation

$$[\boldsymbol{M}]_f^q(R_I) = \{\boldsymbol{M}_f^q(\boldsymbol{x}), \boldsymbol{x}\in R_I\} \tag{36}$$

The notation $\boldsymbol{M}_f^q(\boldsymbol{x})$ represents a vector with the same size as R_f, while the notation $[\boldsymbol{M}]_f^q(R_I)$ represents an n by m matrix with $n = \text{size}(R_I)$ and $m = \text{size}(R_f)$. Other sets can replace R_I in $[\boldsymbol{M}]_f^q(R_I)$ and the same definition applies.

If the points in the set R_I are denoted by $\boldsymbol{x}_1, \boldsymbol{x}_2, \ldots, \boldsymbol{x}_n$ and the points in the set R_f by $\boldsymbol{y}_1, \boldsymbol{y}_2, \ldots, \boldsymbol{y}_m$, then the matrix $[\boldsymbol{M}]_f^q(R_I)$ can be written in expanded form as

$$[\boldsymbol{M}]_f^q(R_I) = \begin{bmatrix} G_f^q(\boldsymbol{x}_1,\boldsymbol{y}_1) & G_f^q(\boldsymbol{x}_1,\boldsymbol{y}_2) & \ldots & G_f^q(\boldsymbol{x}_1,\boldsymbol{y}_m) \\ G_f^q(\boldsymbol{x}_2,\boldsymbol{y}_1) & G_f^q(\boldsymbol{x}_2,\boldsymbol{y}_2) & \ldots & G_f^q(\boldsymbol{x}_2,\boldsymbol{y}_m) \\ \vdots & \vdots & \ddots & \vdots \\ G_f^q(\boldsymbol{x}_n,\boldsymbol{y}_1) & G_f^q(\boldsymbol{x}_n,\boldsymbol{y}_2) & \ldots & G_f^q(\boldsymbol{x}_n,\boldsymbol{y}_m) \end{bmatrix} \tag{37}$$

Similarly, for solid, the notation $\boldsymbol{M}_s^q(\boldsymbol{x})$ represents a vector with m components where $m = 3\times\text{size}(R_s)$, while the notation $[\boldsymbol{M}]_s^q(R_I)$ represents an n by m matrix with $n = \text{size}(R_I)$ and $m = 3\times\text{size}(R_s)$. Again, other sets can replace R_I in $[\boldsymbol{M}]_s^q(R_I)$ and the same definition applies.

If the points in the set R_I are denoted by $\boldsymbol{x}_1, \boldsymbol{x}_2, \ldots, \boldsymbol{x}_n$ and the points in the set R_s by $\boldsymbol{y}_1, \boldsymbol{y}_2, \ldots, \boldsymbol{y}_m$, then the matrix $[\boldsymbol{M}]_s^q(R_I)$ can be written in expanded form as

$$[\boldsymbol{M}]_s^q(R_I) = \begin{bmatrix} G_{s1}^q(\boldsymbol{x}_1,\boldsymbol{y}_1) & G_{s2}^q(\boldsymbol{x}_1,\boldsymbol{y}_1) & G_{s3}^q(\boldsymbol{x}_1,\boldsymbol{y}_1) & \ldots & G_{s1}^q(\boldsymbol{x}_1,\boldsymbol{y}_m) & G_{s2}^q(\boldsymbol{x}_1,\boldsymbol{y}_m) & G_{s3}^q(\boldsymbol{x}_1,\boldsymbol{y}_m) \\ G_{s1}^q(\boldsymbol{x}_2,\boldsymbol{y}_1) & G_{s2}^q(\boldsymbol{x}_2,\boldsymbol{y}_1) & G_{s3}^q(\boldsymbol{x}_2,\boldsymbol{y}_1) & \ldots & G_{s1}^q(\boldsymbol{x}_2,\boldsymbol{y}_m) & G_{s2}^q(\boldsymbol{x}_2,\boldsymbol{y}_m) & G_{s3}^q(\boldsymbol{x}_2,\boldsymbol{y}_m) \\ \vdots & \vdots & \vdots & \ddots & \vdots & \vdots & \vdots \\ G_{s1}^q(\boldsymbol{x}_n,\boldsymbol{y}_1) & G_{s2}^q(\boldsymbol{x}_n,\boldsymbol{y}_1) & G_{s3}^q(\boldsymbol{x}_n,\boldsymbol{y}_1) & \ldots & G_{s1}^q(\boldsymbol{x}_n,\boldsymbol{y}_m) & G_{s2}^q(\boldsymbol{x}_n,\boldsymbol{y}_m) & G_{s3}^q(\boldsymbol{x}_n,\boldsymbol{y}_m) \end{bmatrix} \tag{38}$$

Now, the global system of equations can be written as

$$\begin{bmatrix} [\boldsymbol{M}]_f^{v}(R_T) & [\boldsymbol{0}] \\ [\boldsymbol{M}]_f^{u_3}(R_I) & -[\boldsymbol{M}]_s^{u_3}(R_I) \\ [\boldsymbol{M}]_f^{p}(R_I) & [\boldsymbol{M}]_s^{\sigma_{33}}(R_I) \\ [\boldsymbol{0}] & [\boldsymbol{M}]_s^{\sigma_{23}}(R_I) \\ [\boldsymbol{0}] & [\boldsymbol{M}]_s^{\sigma_{31}}(R_I) \\ [\boldsymbol{0}] & [\boldsymbol{M}]_s^{\sigma_{nn}}(R_H) \\ [\boldsymbol{0}] & [\boldsymbol{M}]_s^{\sigma_{x2n}}(R_H) \\ [\boldsymbol{0}] & [\boldsymbol{M}]_s^{\sigma_{nt}}(R_H) \end{bmatrix} \cdot \begin{Bmatrix} \boldsymbol{A}_f \\ \boldsymbol{A}_s \end{Bmatrix} = \begin{Bmatrix} \boldsymbol{v}_0 \\ \boldsymbol{0} \\ \boldsymbol{0} \\ \boldsymbol{0} \\ \boldsymbol{0} \\ \boldsymbol{0} \\ \boldsymbol{0} \\ \boldsymbol{0} \end{Bmatrix} \tag{39}$$

The above system of equations contains n equations in terms of n unknowns where $n = \text{size}(R_T) + 4\times\text{size}(R_I) + 3\times\text{size}(R_H)$.

3. The windowing technique

The DPSM model presented in Section 2 requires evaluation of the Green's function between many pairs of source and target points. Let us consider the configuration shown in Fig. 6 where a collection of source points located on the upper plane are generating the field at a collection of target points located on the lower plane. Then, in order to build the DPSM model, the Green's function between each pair of source and target points needs to be evaluated. If for each plane shown in Fig. 6 the number of points along the two sides or edges of the plane are n_1 and n_2, then the total number of points on each plane is $n_1 n_2$, and a total number of $(n_1 n_2)^2$ evaluations for the Green's function are required. When increasing the resolution of the model in terms of n_1 and n_2, the number of evaluations for the Green's function can rapidly grow, and make DPSM model computationally very expensive. This is particularly

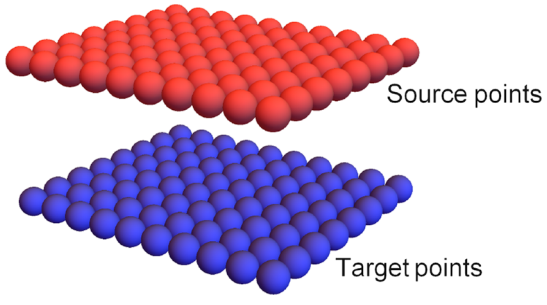

Fig. 6. Planes of source and target points in parallel.

important for anisotropic solids where each evaluation of the Green's function requires a numerical integration.

In an effort to reduce this computational cost, an improvement called "windowing technique" has been recently suggested by Fooladi and Kundu [38]. The main idea behind the windowing technique is to exploit the repetitive pattern of relative positions of target and source points in a structured grid, in order to reduce the number of evaluations for the Green's function. In [38], the windowing technique was presented in the absence of a hole. It was mentioned that for the configuration of two parallel planes shown in Fig. 6 the windowing technique reduces the number of evaluations for the Green's function from $(n_1 n_2)^2$ to $(2n_1-1)(2n_2-1)$ which is considerable reduction (e.g. from 160 000 to 1521 for $n_1 = n_2 = 20$). In the case when an inclusion like a hole is present in the domain, the repetitive pattern of the grid is disturbed, but a considerable portion of domain may remain intact, and the use of the windowing technique can still be very beneficial.

In the following the use of windowing technique in the presence of an inclusion (e.g. a hole) is described. Let us assume the points in planes of Fig. 6 are distanced from their neighbors by Δx_1 and Δx_2 along the two orthogonal directions parallel to the two edges of the plane, and the distance between the two planes is Δx_3. Then similar to the case without a hole, a larger plane of target points is constructed by placing $(2n_1-1)$ and $(2n_2-1)$ points along each edge of the plane with distances Δx_1 and Δx_2 respectively. This extended plane is shown in Fig. 7. Since the number of divisions are odd, there is a point exactly at the center of this plane. A source point is defined at distance Δx_3 above the center of this plane. The Green's function between this individual source point and all the target points on the extended plane are computed and stored in table.

Next, when the Green's function between the sets of source and target points in the original configuration shown in Fig. 6 are required, it is first checked if they are already computed and stored in the table. If there is no disturbance (e.g. a hole) in the structured grid, all Green's functions should be available in the stored table. Otherwise, a portion of them are available, and the rest should be evaluated. This correspondence is verified in the following manner.

Let us first consider the case where there is no disturbance (e.g. a hole) and all source and target points are placed in a completely structured grid. Assume a pair of integer numbers $(i_1,\ i_2)$ is assigned to a point on a plane where i_1 and i_2 are the number of points measured along the plane edges from a corner chosen as $(1,\ 1)$ to the point with $(i_1,\ i_2)$. In other words, $(i_1,\ i_2)$ is an integer coordinate for which the unit lengths are Δx_1 and Δx_2. Now, the Green's function between a source point with coordinate $(i_1,\ i_2)$ and a target point with coordinate $(j_1,\ j_2)$ in the original configuration shown in Fig. 6 is identical to the Green's function for a target point with coordinate $(n_1 + j_1 - i_1,\ n_2 + j_2 - i_2)$ on the extended plane shown in Fig. 7. This correspondence reduces the number of evaluations for the Green's function from $(n_1 n_2)^2$ to $(2n_1-1)(2n_2-1)$ which can be a considerable reduction for large n_1 and n_2.

In the above description it was assumed that the grid is perfectly structured. When an inclusion like a hole disturbs this structured grid, some of the point pairs may not have a correspondence on the extended plane shown in Fig. 7. In that case, for each pair of points in the original configuration, it should first be checked if it has integer coordinates $(i_1,\ i_2)$, so that it can be associated to the extended plane. Therefore, the following algorithm is implemented.

1. Get the coordinates of the the source and target points on the two parallel planes in the original configuration, shown in Fig. 6.
2. Compute the distances Δx_1 and Δx_2 between neighboring points on a plane, and the distance Δx_3 between the two parallel planes.
3. Construct the extended plane of target points shown in Fig. 7. Place a source point above the center of the plane with distance Δx_3 from the plane. Compute the Green's function between this source point and all target points on the extended plane and store them in an array named $\boldsymbol{A}$.
4. Loop over the pairs of source and target points in the original configuration shown in Fig. 6. For each pair, get the real coordinates (x_1, x_2) of the source and (y_1, y_2) of the target points. Compute the relative coordinate $(y_1-x_1,\ y_2-x_2)$, and then the scaled coordinate $(\frac{y_1-x_1}{\Delta x_1},\ \frac{y_2-x_2}{\Delta x_2})$. Check if the scaled coordinate is close enough to an integer coordinate (i_1, i_2) within a pre-specified tolerance. If the answer is yes, pick the Green's function from the array $\boldsymbol{A}$ at location $(n_1 + j_1 - i_1,\ n_2 + j_2 - i_2)$. Otherwise, compute the Green's function.

As can be seen from the above algorithm, when the grid is not completely structured, an extra amount of computation is required to see whether a pair of points in the original configuration matches with the extended plane of target points. Also, some of the points on the extended plane may never be used while their Green's functions are already evaluated. These may add an extra amount of computational burden to the problem. However, our experiment with windowing technique confirmed that the windowing technique is still very effective in reducing the computational time and is well worth to use even in the presence of an inclusion. It should also be mentioned that some pairs of points outside of the truncated structured grid (e.g. new points on hole surface) may find correspondence on the extended plane once they are automatically tested for having an integer coordinate. In any case, it may be helpful to have this capability included in the code, and then add a control key to be able to turn it on and off for different parts of the solution domain based on requirements of the problem configuration and type of the Green's function.

4. The Green's function for an ideal fluid

In Eq. (4) of Section 2, the vector $\boldsymbol{M}_f^q$ was defined based on the Green's function in fluid G_f^q. In this section the Green's function in fluid for a number of quantities q will be briefly presented from [1]. These quantities are displacement, velocity and pressure in the fluid.

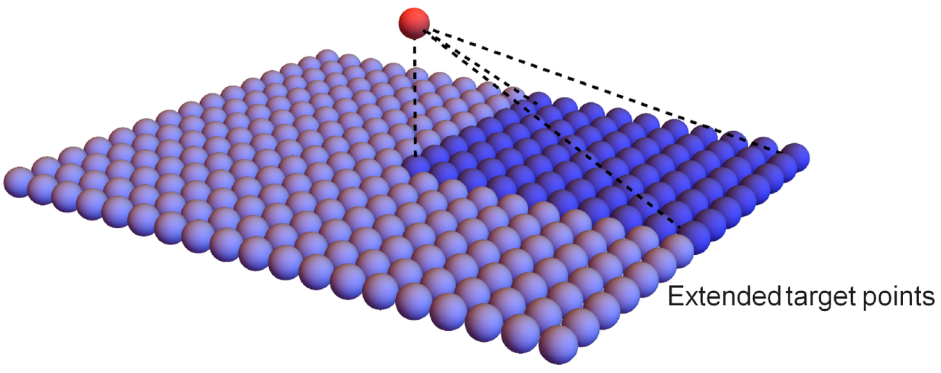

Fig. 7. The extended plane of target points used for windowing technique.

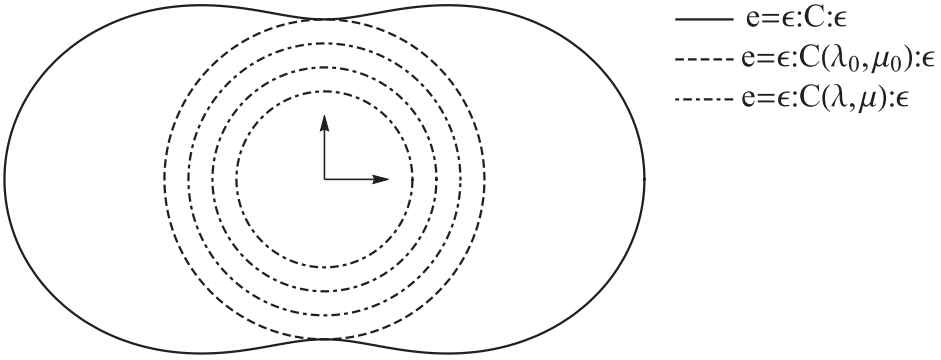

Fig. 8. Analogy of surface defined by a constant strain energy density function to elliptical curves. $\boldsymbol{C}$ is the original anisotropic stiffness tensor, $\boldsymbol{C}(\lambda, \mu)$ is an isotropic stiffness tensor defined based on the Lame constants λ and μ, and $\boldsymbol{C}(\lambda_0, \mu_0)$ is the isotropic stiffness tensor best representing the original anisotropic stiffness tensor.

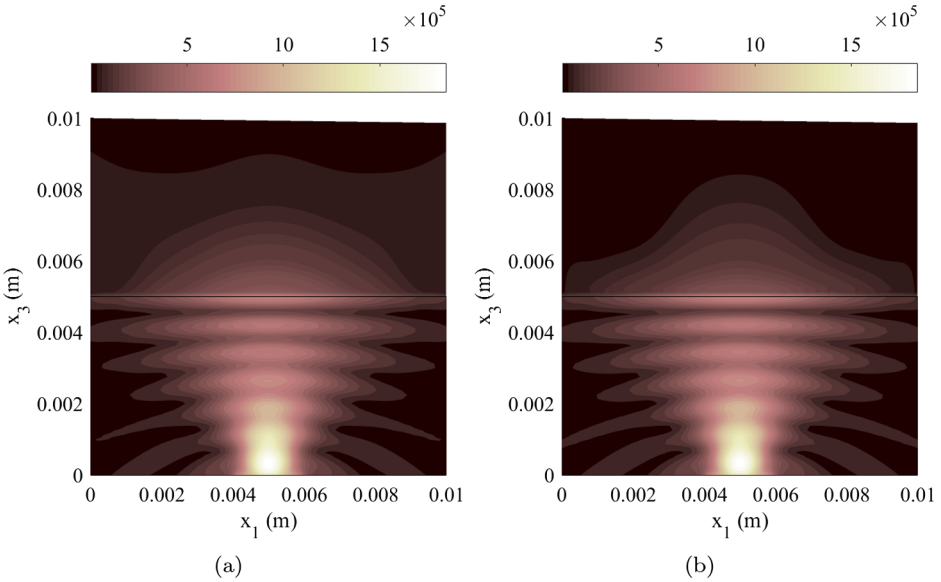

Fig. 9. Distribution of pressure for fluid and the stress component σ_{33} for solid on central x_1–x_3 plane for a transversely isotropic half-space containing no hole: (a) x_1 as the axisymmetric direction, (b) x_2 as the axisymmetric direction.

The fluid is assumed to be perfect. A perfect fluid is an isotropic and homogeneous medium which cannot bear any shear stress and the normal stress is the same in all directions.

The Green's function for pressure due to a time harmonic unit source point at $f = \delta(\boldsymbol{x}-\boldsymbol{y})\exp(-\boldsymbol{i}\omega t)$ can be written as

$$G_f^p(\boldsymbol{x}, \boldsymbol{y}) = \frac{\exp(\boldsymbol{i}k_f r)}{4\pi r} \tag{40}$$

where $k_f = \frac{w}{c_f}$ is the wave number and $r = \|\boldsymbol{x}-\boldsymbol{y}\|$.

Green's function for displacement components in i^{th} direction is given as

$$G_f^{u_i}(\boldsymbol{x}, \boldsymbol{y}) = \frac{\exp(\boldsymbol{i}k_f r)}{4\pi\rho\omega^2 r^3}(\boldsymbol{i}k_f r-1)(x_i-y_i) \tag{41}$$

Considering the harmonic time variation of the quantities, the Green's function for the velocity is obtained from the above expression as

$$G_f^{v_i}(\boldsymbol{x}, \boldsymbol{y}) = \frac{\exp(\boldsymbol{i}k_f r)}{4\pi\boldsymbol{i}\rho\omega r^3}(\boldsymbol{i}k_f r-1)(x_i-y_i) \tag{42}$$

Eqs. (40)–(42) can be used in constructing the fluid part of the DPSM model described previously.

5. The Green's function for anisotropic solid

In Eq. (10) of the Section 2, the vector $\boldsymbol{M}_s^q$ was defined based on the Green's function in solid G_s^q. In this section the construction of the Green's function for anisotropic solid done by Wang and Achenbach [47] will be briefly reviewed.

The equations of motion for small deformation in an anisotropic homogeneous medium can be written in terms of displacement components as

$$C_{ijkl}\frac{\partial^2 u_k}{\partial x_j \partial x_l} + f_i = \rho\frac{\partial^2 u_i}{\partial t^2} \tag{43}$$

where C_{ijkl} are components of stiffness tensor, u_i are components of displacement vector, f_i are components of the body force density vector, and ρ is the mass density.

The elastodynamic Green's function $\boldsymbol{G}_s^{u_i}(\boldsymbol{x}, \boldsymbol{y})$ is the solution to the above equation for displacement component u_i at point $\boldsymbol{x}$ when a point force is applied at point $\boldsymbol{y}$. For simplicity, this Green's function is shown by $G_{ij}(\boldsymbol{x}, \boldsymbol{y})$. The time harmonic force and displacement vectors can be written as

$$f_i(\boldsymbol{x}, t) = A_i\delta(\boldsymbol{x}-\boldsymbol{y})\exp(-\boldsymbol{i}\omega t) \tag{44}$$

$$u_i(\boldsymbol{x}, t) = G_{ij}(\boldsymbol{x}, \boldsymbol{y})A_j\exp(-\boldsymbol{i}\omega t) \tag{45}$$

Substituting from Eqs. (44) and (45) into Eq. (43) and canceling out

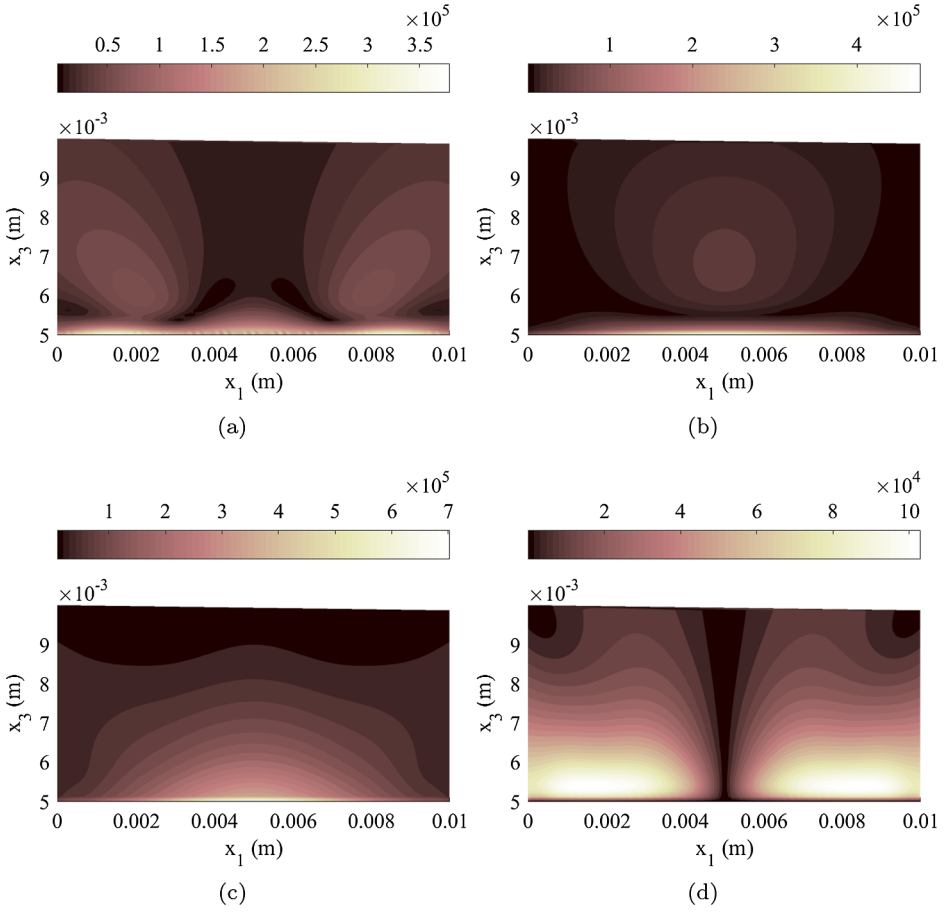

Fig. 10. A transversely isotropic half-space with x_1 as the axisymmetric direction (no hole): the results on the central x_1–x_3 plane for (a) σ_{11}, (b) σ_{22}, (c) σ_{33}, (d) σ_{31}.

the time dependence from both sides of the equation give

$$C_{ijkl}\frac{\partial^2 G_{kp}(\boldsymbol{x},\boldsymbol{y})}{\partial x_j \partial x_l}A_p + \rho\omega^2 G_{ip}(\boldsymbol{x},\boldsymbol{y})A_p = -A_i\delta(\boldsymbol{x}-\boldsymbol{y}) \tag{46}$$

The above set of 3 equations holds for any value of the vector A_p. Therefore, we choose $A_p = \delta_{pq}$ and derive 3 sets of 3 equations for $q = 1, 2, 3$.

$$C_{ijkl}\frac{\partial^2 G_{kq}(\boldsymbol{x},\boldsymbol{y})}{\partial x_j \partial x_l} + \rho\omega^2 G_{iq}(\boldsymbol{x},\boldsymbol{y}) = -\delta_{iq}\delta(\boldsymbol{x}-\boldsymbol{y}) \tag{47}$$

The above system of equations has been solved by Wang and Achenbach [47] using Radon transform. The final solution consists of two parts: the singular part shown by $G^S_{kp}(\boldsymbol{x},\boldsymbol{y})$ and the regular (non-singular) part shown by $G^R_{kp}(\boldsymbol{x},\boldsymbol{y})$. The singular part can be written as

$$G^S_{kp}(\boldsymbol{x},\boldsymbol{y}) = \frac{1}{8\pi^2 r}\int_S K^{-1}_{kp}(\boldsymbol{\xi})dS(\boldsymbol{\xi}) \tag{48}$$

where $K_{ik}(\boldsymbol{\xi}) = C_{ijkl}\xi_l\xi_j$ and S is an oblique circular path in 3D defined by

$$S = \{\xi \in R^3 | \|\boldsymbol{\xi}\| = 1,\ \boldsymbol{\xi}\cdot(\boldsymbol{x}-\boldsymbol{y}) = 0\} \tag{49}$$

The regular part can be written as an integral over a unit sphere as

$$G^R_{kp}(\boldsymbol{x},\boldsymbol{y}) = \frac{\boldsymbol{i}}{16\pi^2}\int_{\|\boldsymbol{n}\|=1}\sum_{m=1}^{3}\frac{\alpha_m E_{km}E_{pm}}{\rho c_m^2}\exp(\boldsymbol{i}\alpha_m\|\boldsymbol{n}\cdot(\boldsymbol{x}-\boldsymbol{y})\|)dS(\boldsymbol{n}) \tag{50}$$

where $K_{ik}(\boldsymbol{n}) = C_{ijkl}n_l n_j$, λ_m $(m = 1, 2, 3)$ are eigenvalues of $\boldsymbol{K}$, $c_m = \sqrt{\lambda_m/\rho}$ and $\alpha_m = \omega/c_m$ are the phase velocity and the wave number associated with eigenvalue λ_m, respectively. Also, $\boldsymbol{E}$ is a matrix with columns representing eigenvectors of $\boldsymbol{K}$. The eigenvalue problem for $\boldsymbol{K}(\boldsymbol{n})$ can be written as

$$K_{ik}E_{km} = \lambda_m E_{im},\ m = 1, 2, 3 \text{ (no sum on } m) \tag{51}$$

The integration domain for the regular part of the solution can be reduced into a hemisphere due to symmetry properties of the integral.

$$G^R_{kp}(\boldsymbol{x},\boldsymbol{y}) = \frac{\boldsymbol{i}}{8\pi^2}\int_{\text{Hemi-sphere}}\sum_{m=1}^{3}\frac{\alpha_m E_{km}E_{pm}}{\rho c_m^2}\exp(\boldsymbol{i}\alpha_m\|\boldsymbol{n}\cdot(\boldsymbol{x}-\boldsymbol{y})\|)dS(\boldsymbol{n}) \tag{52}$$

In Eq. (51) and in the remainder of this paper whenever the index m refers to the number of eigenvalues or eigenvectors or a parameter derived from them, the summation convention does not apply.

5.1. Residue method

Residue method was used by Sales and Gray [49] to evaluate the singular part of the solution shown in Eq. (48). To do so, they converted the integral into an integral from $-\infty$ to $+\infty$ shown below.

$$G^S_{ij}(\theta,\psi) = \frac{1}{4\pi^2 r}\int_{-\infty}^{\infty}\frac{P_{ij}(Z)}{Q(Z)}dZ \tag{53}$$

where $\boldsymbol{P}(Z)$ and $Q(Z)$ are the cofactor and the determinant of the matrix $\boldsymbol{K}$, respectively. Next, the above integral is evaluated by residue method as

$$G^S_{ij}(\theta,\psi) = \frac{\boldsymbol{i}}{2\pi r}\sum_{n=1}^{3}\text{Residue}\left(\frac{P_{ij}(Z)}{Q(Z)}\right)\Bigg|_{z=\lambda_n} = \frac{\boldsymbol{i}}{2\pi r}\sum_{n=1}^{3}\frac{p(\lambda_n)}{Q_n(\lambda_n)} \tag{54}$$

where λ_n, $n = 1, 2, 3$ represent the three roots of $Q(Z)$ in the upper half plane, and

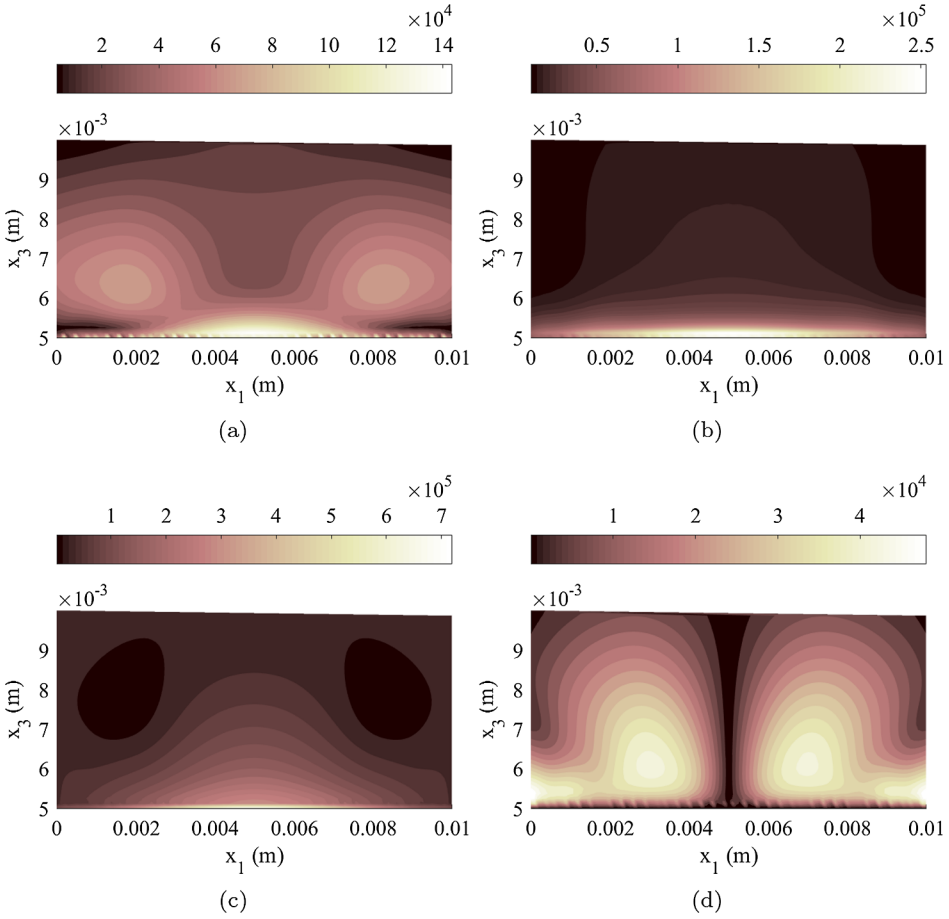

Fig. 11. A transversely isotropic half-space with x_2 as the axisymmetric direction (no hole): the results on the central x_1–x_3 plane for (a) σ_{11}, (b) σ_{22}, (c) σ_{33}, (d) σ_{31}.

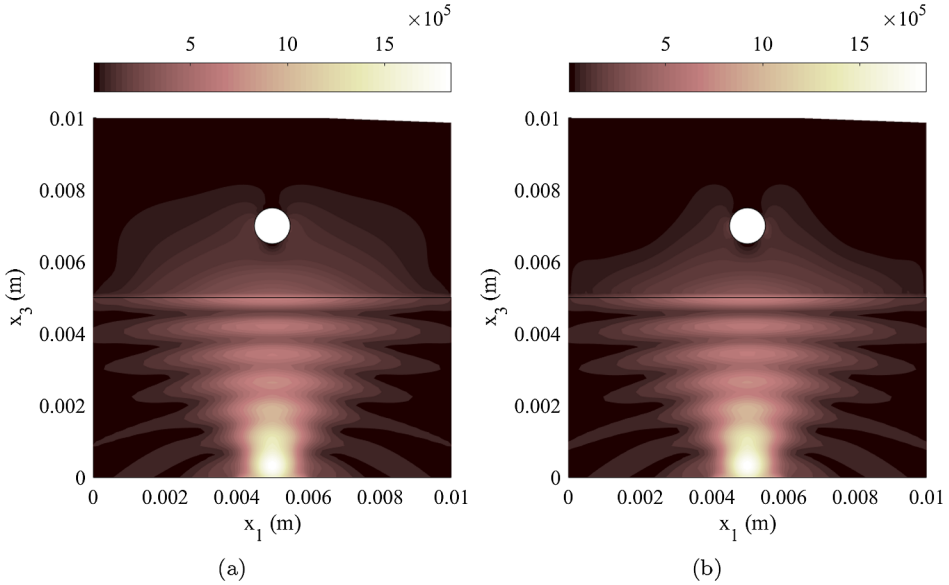

Fig. 12. Distribution of pressure for fluid and the stress component σ_{33} for solid on central x_1–x_3 plane for a transversely isotropic half-space containing a hole of radius $r = 0.5$ mm: (a) x_1 as the axisymmetric direction, (b) x_2 as the axisymmetric direction.

$$Q_n(Z) = \frac{Q(Z)}{\lambda - Z_n} \tag{55}$$

In the above formulation it is assumed that three roots are distinct and simple poles. In the case of higher order poles either the above formulation needs to be modified or as mentioned in [49] one can slightly perturb the coordinates of the point with the repeated roots in different directions, and then take the average of the solutions at the perturbed points. For an anisotropic material repeated roots may happen only at few isolated points. But for an isotropic materials, roots are repeated at any point and the above algorithm is not applicable any more. However, for isotropic materials the closed form solution is

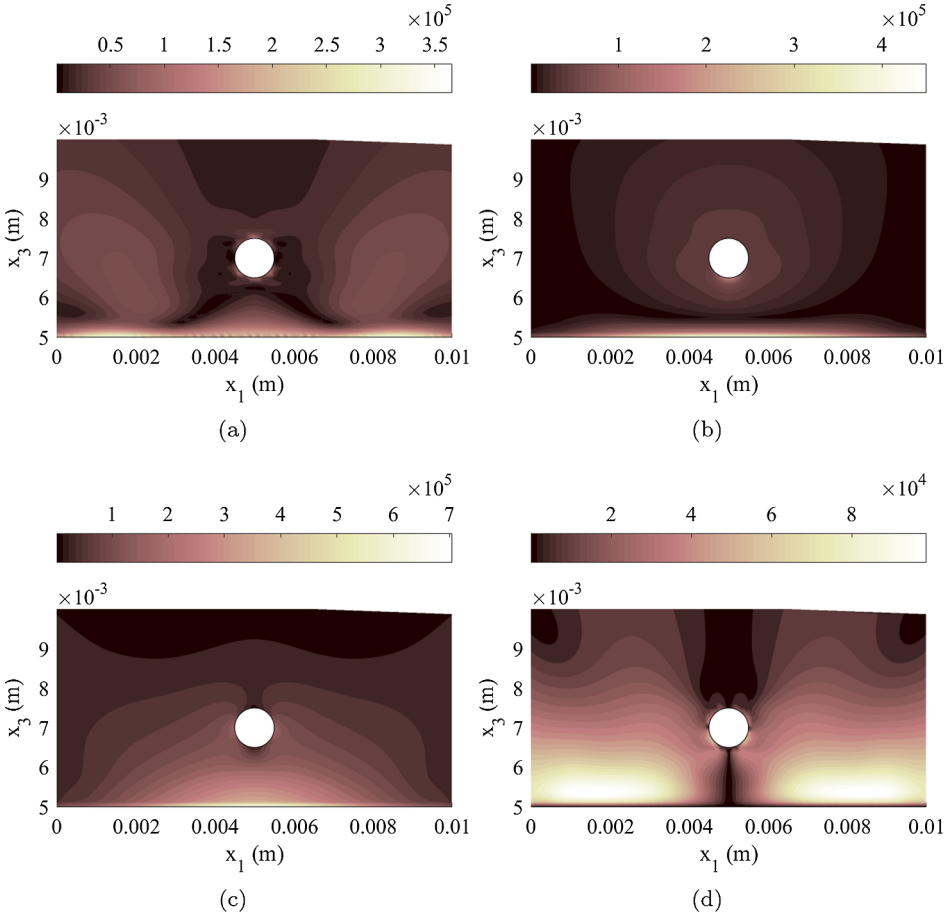

Fig. 13. A transversely isotropic half-space with x_1 as the axisymmetric direction containing a hole with radius $r = 0.5$ mm: the results on the central x_1–x_3 plane for (a) σ_{11}, (b) σ_{22}, (c) σ_{33}, (d) σ_{31}.

available and there is no need to perform integration.

Applications of the Green's function, such as BEM and DPSM, require the derivatives of the displacement Green's function to calculate strain and stress tensors. First, the derivatives of the singular part of the solution with respect to the spherical coordinates are taken, then the results are transformed back to the Cartesian coordinate system. The derivative of the Eq. (54) with respect to the radial coordinate r is

$$G^S_{ij,r} = -\frac{1}{8\pi^2 r^2} G^S_{ij} = -\frac{\boldsymbol{i}}{2\pi r^2} \sum_{n=1}^{3} \frac{P(\lambda_n)}{Q_n(\lambda_n)} \tag{56}$$

The derivative of Eq. (53) with respect to the polar angle θ is

$$G^S_{ij,\theta} = \frac{1}{4\pi^2 r} \int_{-\infty}^{\infty} \frac{P_{ij,\theta}(Z)Q(Z) - P_{ij}(Z)Q_{,\theta}(Z)}{Q(Z)^2} dZ \tag{57}$$

The application of the residue theorem gives

$$G^S_{ij,\theta} = \frac{1}{4\pi^2 r} \sum_{n=1}^{3} \frac{\partial}{\partial Z} \left(\frac{P_{ij,\theta}(Z)Q(Z) - P_{ij}(Z)Q_{,\theta}(Z)}{Q(Z)^2} \right) \Bigg|_{Z=\lambda_n} \tag{58}$$

Substituting $Z = \lambda_n$ and considering that $Q(\lambda_n) = 0$, the above expression is reduced to

$$G^S_{ij,\theta} = \frac{\boldsymbol{i}}{2\pi r} \sum_{n=1}^{3} \left[\left(\frac{2Q_{n,Z}(\lambda_n)Q_{,\theta}(\lambda_n) - Q_n(\lambda_n)Q_{,\theta Z}(\lambda_n)}{Q_n(\lambda_n)^3} \right) P_{jk}(\lambda_n) + \frac{Q_{,Z}(\lambda_n)}{Q_n(\lambda_n)^2} P_{jk,\theta}(\lambda_n) - \frac{Q_{,\theta}(\lambda_n)}{Q_n(\lambda_n)^2} P_{jk,Z}(\lambda_n) \right] \tag{59}$$

The derivative with respect to the azimuthal angle ψ is taken in a similar way which gives the same result as the above expression with θ being replaced by ψ. There is a typo in Eq. (20) of the paper by Sales and Gray [49], which has been corrected in the above equation [Eq. (59)] by Fooladi and Kundu [38].

5.2. Reduction of integration domain for transversely isotropic materials

Unlike the singular part of the solution the regular part is a two dimensional integral on the surface of a unit sphere. Thus, the majority of the computational cost is related to the integration of the regular part. The integration domain can be reduced to a hemi sphere, as was shown in Eq. (52), due to symmetry property of the integrand. For a general anisotropic material no more simplification seems to be possible. But, for transversely isotropic materials, Fooladi and Kundu [38] developed a technique to reduce the integration domain into a quarter sphere which is very effective in reducing computational cost. In this section, this formulation is briefly presented.

First, the original coordinate system $x_1x_2x_3$ is rotated by transformation matrix $\boldsymbol{Q}$ to a new coordinate system $x_1'x_2'x_3'$, such that x_3' is the principal direction of the transversely isotropic material and the projection of the vector $\boldsymbol{x}$–$\boldsymbol{y}$ on $x_1'x_2'$ plane lies along the x_1' axis. The components of vector $\boldsymbol{x}$–$\boldsymbol{y}$ in the rotated coordinate system can be written as

$$\boldsymbol{x}'-\boldsymbol{y}' = \boldsymbol{Q}\cdot(\boldsymbol{x}-\boldsymbol{y}) \tag{60}$$

The regular part of elastodynamic Green's function can be written as an integral over a quarter-sphere in the rotated coordinate system,

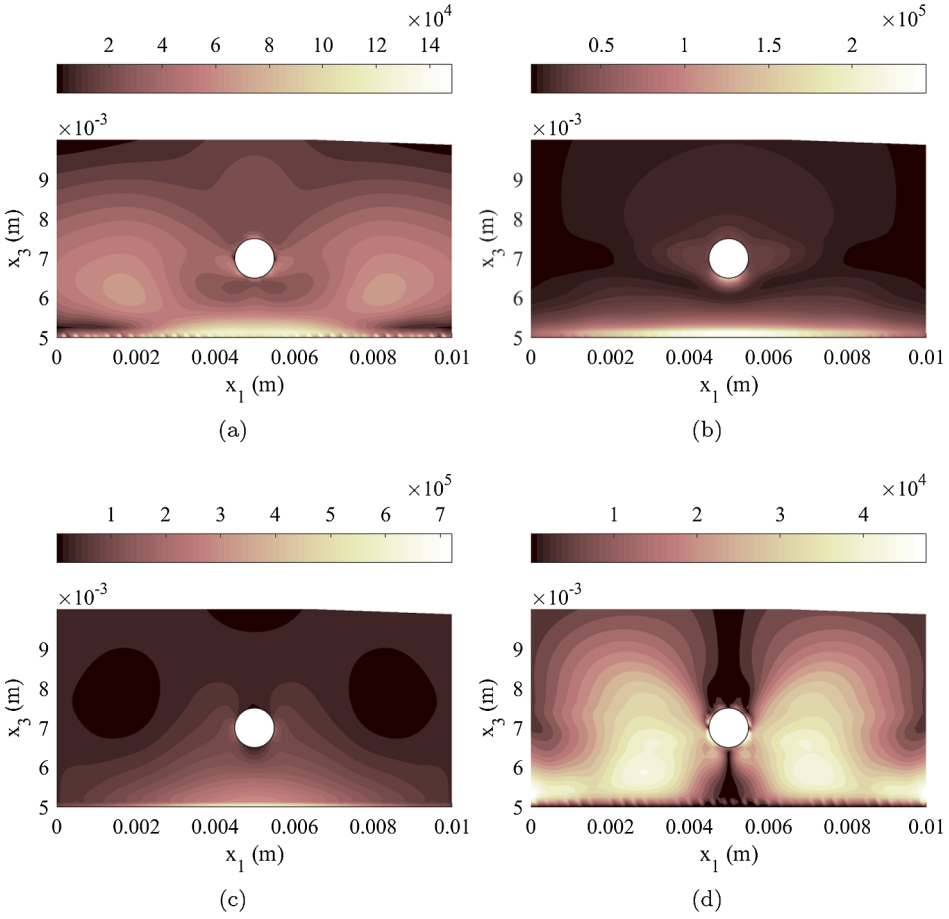

Fig. 14. A transversely isotropic half-space with x_2 as the axisymmetric direction containing a hole with radius $r = 0.5$ mm: the results on the central x_1–x_3 plane for (a) σ_{11}, (b) σ_{22}, (c) σ_{33}, (d) σ_{31}.

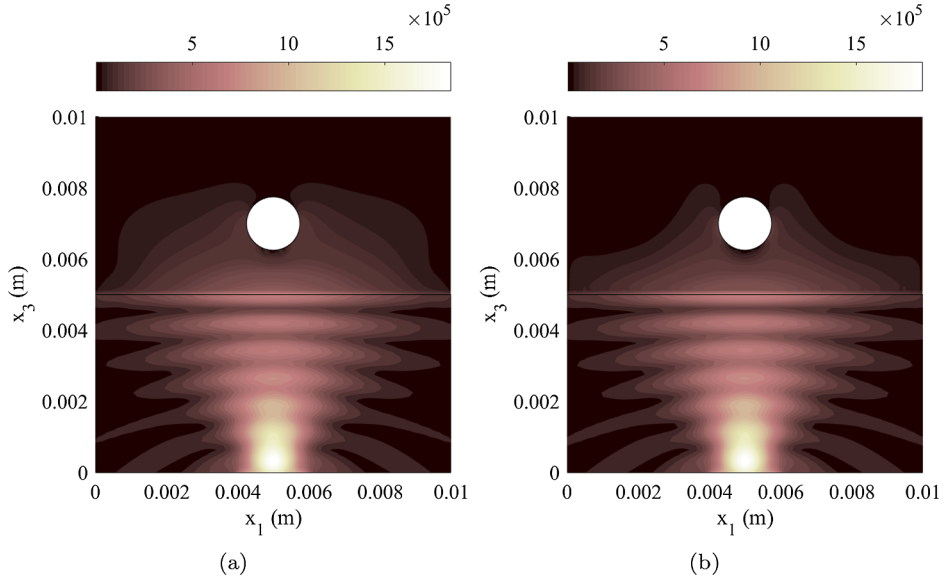

Fig. 15. Distribution of pressure for fluid and the stress component σ_{33} for solid on central x_1–x_3 plane for a transversely isotropic half-space containing a hole of radius $r = 0.75$ mm: (a) x_1 as the axisymmetric direction, (b) x_2 as the axisymmetric direction.

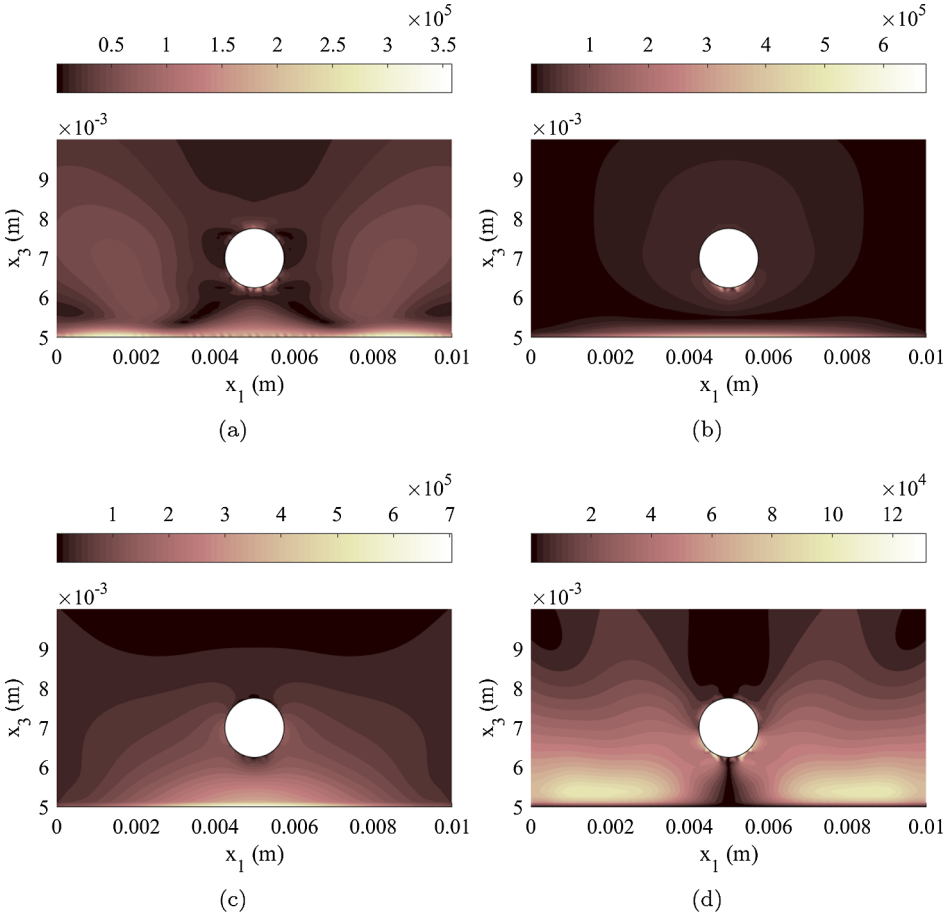

Fig. 16. A transversely isotropic half-space with x_1 as the axisymmetric direction containing a hole with radius $R = 0.75$ mm: the results on the central x_1–x_3 plane for (a) σ_{11}, (b) σ_{22}, (c) σ_{33}, (d) σ_{31}.

$$G'^{R}_{ij}(\boldsymbol{x},\boldsymbol{y}) = \frac{\boldsymbol{i}}{8\pi^2}\int_0^{\pi/2}\int_0^{\pi}\frac{\alpha_m}{\rho c_m^2}\sum_{ij}^{m}(\theta,\phi)\exp(\boldsymbol{i}\alpha_m|\boldsymbol{n}'\cdot(\boldsymbol{x}'-\boldsymbol{y}')|)\sin\phi d\theta d\phi \tag{61}$$

where θ and ϕ are polar and azimuthal angles respectively, and

$$\sum_{ij}^{m}(\theta,\phi) = 2\begin{bmatrix}(E'_{1m})^2(\theta,\phi) & 0 & (E'_{1m}E'_{3m})(\theta,\phi)\\ 0 & (E'_{2m})^2(\theta,\phi) & 0\\ (E'_{1m}E'_{3m})(\theta,\phi) & 0 & (E'_{3m})^2(\theta,\phi)\end{bmatrix} \tag{62}$$

Similarly, the derivative of the regular part of the solution can be written in the rotated coordinates system as

$$\frac{\partial G'^{R}_{ij}(\boldsymbol{x},\boldsymbol{y})}{\partial x'_k} = -\frac{1}{8\pi^2}\int_0^{\pi/2}\int_0^{\pi}\frac{n'_q\alpha_m^2}{\rho c_m^2}A^m_{ij}(\theta,\phi)\,\mathrm{sign}(\boldsymbol{n}'\cdot(\boldsymbol{x}'-\boldsymbol{y}'))\exp(\boldsymbol{i}\alpha_m|\boldsymbol{n}'\cdot(\boldsymbol{x}'-\boldsymbol{y}')|)\sin\phi\,d\theta\,d\phi \tag{63}$$

where

$$A^m_{ij} = \begin{cases}\sum^m_{ij} & \text{for } k = 1, 3\\ \Pi^m_{ij} & \text{for } k = 2\end{cases} \tag{64}$$

and

$$\Pi^m_{ij}(\theta,\phi) = 2\begin{bmatrix}0 & (E'_{1m}E'_{2m})(\theta,\phi) & 0\\ (E'_{1m}E'_{2m})(\theta,\phi) & 0 & (E'_{2m}E'_{3m})(\theta,\phi)\\ 0 & (E'_{2m}E'_{3m})(\theta,\phi) & 0\end{bmatrix} \tag{65}$$

The back transformation of the regular part and its derivatives from the rotated coordinate system to the original coordinate system can be written as

$$G^R_{ij} = Q_{im}Q_{jn}G'^{R}_{mn} \tag{66}$$

and

$$\frac{\partial G^R_{ij}}{\partial x_k} = Q_{kl}Q_{im}Q_{jn}\frac{\partial G'^{R}_{mn}}{\partial x'_l} \tag{67}$$

Once, the regular part and its derivatives are computed on the quarter-sphere in the rotated coordinate system, they can be transformed back to the original coordinate system using Eqs. (66) and (67).

6. Calibration of integration resolution

In DPSM method, the geometrical features (e.g. traducer surface, fluid-solid interface, etc.) are modeled as a collection of relatively large number of discrete points. The interaction between these features is then evaluated by superimposing the effect of each source point on each target point via computation of the Green's function. Such modeling strategy requires repetitive evaluation of the Green's function for a relatively large number of times, and may become computationally intensive in the case when the Green's function needs to be evaluated numerically (e.g. for anisotropic solids).

The elastodynamic Greens function consists of singular and regular parts. The singular part is in the form of a 1D integral and can be converted to algebraic terms. But the regular part is in the form of a 2D integral, and requires a relatively large number of integration points in each direction. The regular part is the main cause of increasing the time of computations.

On one hand the numerical integration of regular part should be fine enough to uphold the overall accuracy of the DPSM model, but on the

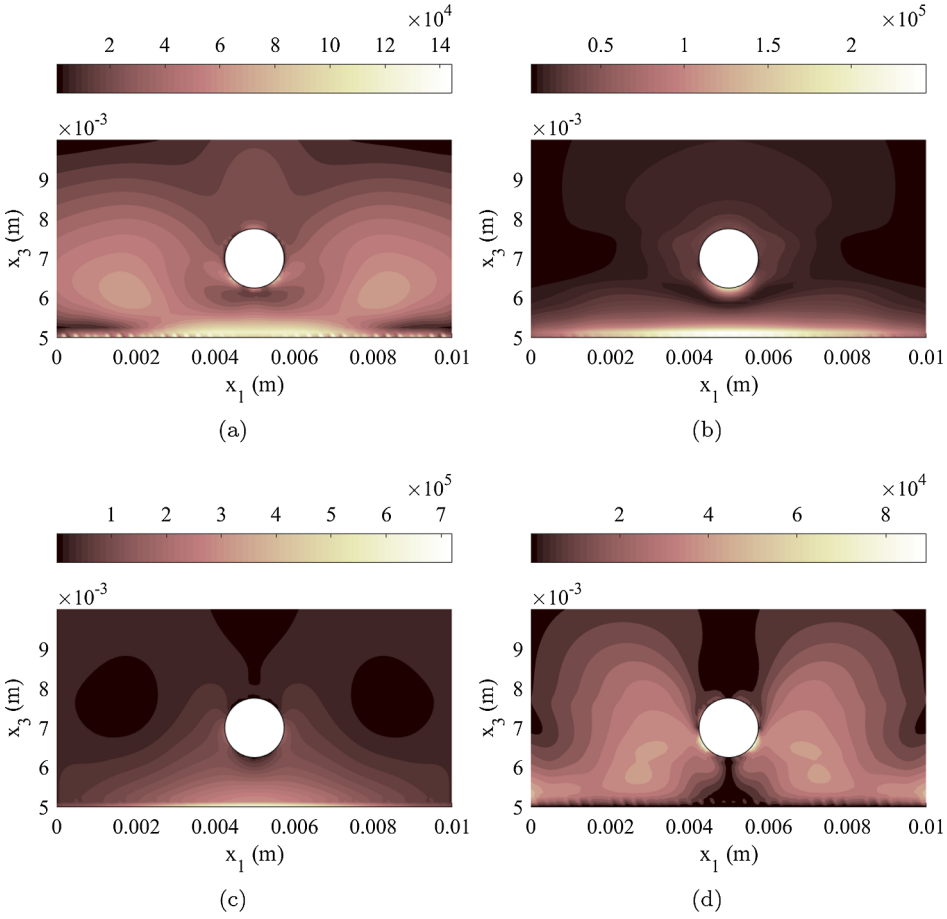

Fig. 17. A transversely isotropic half-space with x_2 as the axisymmetric direction containing a hole with radius $R = 0.75$ mm: the results on the central x_1–x_3 plane for (a) σ_{11}, (b) σ_{22}, (c) σ_{33}, (d) σ_{31}.

other hand it should be coarse enough to keep the computational time affordable and convenient.

In order to achieve a balance between time and accuracy, a strategy for calibrating the numerical integration of the regular part of the elastodynamic Green's function is suggested here. This calibration technique is devised based on the following observation obtained from experimenting and also from intuitive analysis of the equations: the accuracy of the integration decreases by increasing the distance between the pair of source and target points, and also by decreasing the stiffness of the system while all other properties are held constant. Based on this observation, a multi-resolution integration technique is planned which sets automatically an optimum number of integration points for a finite number of distance intervals between the source and target points. Different steps of this algorithm are listed below:

1. Compute an isotropic equivalent of the original anisotropic stiffness matrix
2. Identify the maximum distance r_{max} between the source and target points in the DPSM model.
3. Divide the distance range to a number of intervals $0 = r_0 < r_1 < r_2 < ... < r_n = r_{\max}$ where n is a user provided number.
4. For each r_i where $i = 1, ..., n$ find an optimum resolution for the 2D integration $\{p_i, q_i\}$, by comparing the analytical and numerical solutions for the equivalent isotropic stiffness, and requiring that the error in the numerical solution falls below a threshold specified by the user.
5. Deliver the calibration results $\{r_i, p_i, q_i\}$ where $i = 1, ..., n$ to the DPSM model.
6. In computing the Green's function for a pair of source and target points with distance r, find the interval where r belongs ($r_{i-1} < r \leqslant r_i$), and use the corresponding resolution for it, $\{p_i, q_i\}$.

The step one above requires computation of an equivalent isotropic stiffness matrix from the original stiffness matrix which is anisotropic. This step is explained in more details in the following. As mentioned before, it was observed that the accuracy of integration decreases when the components of the stiffness matrix are made smaller. In order to quantify this observation, we make the assumption that having a less stiff system is equivalent to having a smaller energy density function for a fixed amount of strain. The strain energy density function e for a linear anisotropic solid can be written as

$$e = \frac{1}{2} \; {}^{\mathrm{T}}\cdot\boldsymbol{C}\cdot \tag{68}$$

where and $\boldsymbol{C}$ are 6×1 strain vector and 6×6 stiffness matrix in Voigt notation, respectively.

An isotropic stiffness matrix can be written as a function of two independent constants. Let us denote an isotropic stiffness matrix by $\boldsymbol{C}(\lambda, \mu)$ where λ and μ are the Lame constants. We are looking for particular values of Lame constants λ_0 and μ_0 for which the isotropic stiffness matrix $\boldsymbol{C}(\lambda_0, \mu_0)$ best represents the original anisotropic stiffness matrix $\boldsymbol{C}$.

Let us define the set $S^{\lambda,\mu}$ as

$$S^{\lambda,\mu} = \{(\lambda, \mu): (\; {}^{\mathrm{T}}\cdot\boldsymbol{C}(\lambda, \mu)\cdot \;) \leqslant (\; {}^{\mathrm{T}}\cdot\boldsymbol{C}\cdot \;), \forall \quad \in S\} \tag{69}$$

where the set S represents the space of 6×1 vectors. Then, the Lame constants λ_0, μ_0 of equivalent isotropic stiffness matrix $\boldsymbol{C}(\lambda_0, \mu_0)$ are determined based on the following two conditions

$$(\ ^{T}\cdot \boldsymbol{C}(\lambda_0, \mu_0)\cdot \ ) \leqslant (\ ^{T}\cdot \boldsymbol{C}\cdot \ ), \quad \forall \quad \in S \tag{70}$$

$$(\ ^{T}\cdot \boldsymbol{C}(\lambda_0, \mu_0)\cdot \ ) \geqslant (\ ^{T}\cdot \boldsymbol{C}(\lambda, \mu)\cdot \ ), \quad \forall \quad \in S, \ \forall \ (\lambda, \mu) \in S^{\lambda,\mu} \tag{71}$$

The first condition, Eq. (70), means that the strain energy density function for $\boldsymbol{C}(\lambda_0, \mu_0)$ is less than or equal to that of $\boldsymbol{C}$. This ensures that the error in the numerical integration for $\boldsymbol{C}(\lambda_0, \mu_0)$ provides an upper bound for that of $\boldsymbol{C}$. The second condition, Eq. (71), means that the strain energy density function for $\boldsymbol{C}(\lambda_0, \mu_0)$ is as close as possible to the anisotropic one, and ensures the upper bound to be as small as possible.

In the following, a visual interpretation of the conditions (70) and (71) are presented. First, let us normalize strain vector . It can be verified that if conditions (70) and (71) hold for every $\in S$, then they also hold for every $\in S$ for which $\| \ \| = 1$, and vice versa. Therefore the conditions for finding the equivalent isotropic stiffness matrix can be rewritten as

$$(\ ^{T}\cdot \boldsymbol{C}(\lambda_0, \mu_0)\cdot \ ) \leqslant (\ ^{T}\cdot \boldsymbol{C}\cdot \ ), \forall \quad \in S: \ \| \ \| = 1 \tag{72}$$

$$(\ ^{T}\cdot \boldsymbol{C}(\lambda_0, \mu_0)\cdot \ ) \geqslant (\ ^{T}\cdot \boldsymbol{C}(\lambda, \mu)\cdot \ ), \quad \forall \quad \in S: \ \| \ \| = 1, \ \forall \ (\lambda, \mu) \in S^{\lambda,\mu} \tag{73}$$

The constraint $\| \ \| = 1$ defines a sphere in S, and the above conditions are comparing the strain energy density function on the surface of this sphere. In order to have a visual plot of this interpretation on a 2D surface, let us replace $\boldsymbol{C}$ and with a 2×2 matrix $\boldsymbol{B}$ and a 2×1 vector $\boldsymbol{x}$, respectively. Then, we are dealing with elliptical curves in 2D space (some restrictions apply on $\boldsymbol{B}$). We may also assume that reduction of an ellipse to a simple circle corresponds to the reduction of anisotropic stiffness matrix to an isotropic one. Now, in analogy with $\| \ \| = 1$, we assume $\|\boldsymbol{x}\| = 1$, and plot the curves $(\boldsymbol{x}^{T}\cdot \boldsymbol{B}\cdot \boldsymbol{x})\boldsymbol{x}$ on a 2D plot, as shown in Fig. 8. In this figure, the equivalent isotropic stiffness matrix corresponds to the circle which is as close as possible to the non-circular curve corresponding to the anisotropic stiffness matrix, while not crossing it.

Now, let us use the inequalities (70) and (71) to determine the Lame constants λ_0 and μ_0 for the equivalent isotropic stiffness matrix $\boldsymbol{C}(\lambda_0, \mu_0)$. The first condition, Eq. (70), can be seen as a requirement to ensure convergence of the numerical integration for the anisotropic Green's function within the pre-specified tolerance. Therefore, in the following the first condition will be enforced in a strict manner. The second condition, Eq. (71), however is only defined to maintain the computational efficiency of numerical integration. Therefore, in the following the second condition will be satisfied only in an approximate manner by choosing the Lame constants λ_0 and μ_0 as large as possible.

The first condition, Eq. (70), can be rewritten as

$$(\ ^{T}\cdot \boldsymbol{A}(\lambda_0, \mu_0)\cdot \ ) \geqslant 0 \tag{74}$$

where $\boldsymbol{A}(\lambda_0, \mu_0) = \boldsymbol{C}-\boldsymbol{C}(\lambda_0, \mu_0)$.

Eq. (74) means $\boldsymbol{A}(\lambda_0, \mu_0)$ is a positive semi-definite matrix. In order for a matrix to be positive semi-definite, all upper left sub-matrices whitin this matrix should have non-negative determinants [50]. By applying this condition to the matrix $\boldsymbol{A}(\lambda_0, \mu_0)$, the values of Lame constants λ_0 and μ_0 can be computed.

The details of such procedure is shown below for an orthotropic material in which the normal and shear stresses are decoupled. The stiffness matrix of an orthotropic material has the the following general structure.

$$\boldsymbol{C} = \begin{bmatrix} c_{11} & c_{12} & c_{13} & & & \\ c_{12} & c_{22} & c_{23} & & & \\ c_{13} & c_{23} & c_{33} & & & \\ & & & c_{44} & & \\ & & & & c_{55} & \\ & & & & & c_{66} \end{bmatrix} \tag{75}$$

The matrix $\boldsymbol{A}(\lambda_0, \mu_0)$ inherits the same structure of zero entries from the above matrix. This allows to break down the requirement for the positive semi-definiteness of $\boldsymbol{A}(\lambda_0, \mu_0)$ into requiring positive semi-definiteness for the following two sub-matrices where one accounts for normal deformations and the other one for shear deformations.

$$\boldsymbol{A}_1 = \begin{bmatrix} c_{11}-(\lambda_0 + 2\mu_0) & c_{12}-\lambda_0 & c_{13}-\lambda_0 \\ c_{12}-\lambda & c_{22}-(\lambda_0 + 2\mu_0) & c_{23}-\lambda_0 \\ c_{13}-\lambda_0 & c_{23}-\lambda_0 & c_{33}-(\lambda_0 + 2\mu_0) \end{bmatrix} \tag{76}$$

$$\boldsymbol{A}_2 = \begin{bmatrix} c_{44}-\mu_0 & & \\ & c_{55}-\mu_0 & \\ & & c_{66}-\mu_0 \end{bmatrix} \tag{77}$$

The matrix $\boldsymbol{A}(\lambda_0, \mu_0)$ is positive semi-definite if and only if matrices $\boldsymbol{A}_1$ and $\boldsymbol{A}_2$, shown above, are positive semi-definite. The matrix $\boldsymbol{A}_2$ is a diagonal matrix and is positive semi-definite if all diagonal entries are non-negative. Therefore,

$$\mu_0 \leqslant c_{44} \tag{78}$$

$$\mu_0 \leqslant c_{55} \tag{79}$$

$$\mu_0 \leqslant c_{66} \tag{80}$$

The matrix $\boldsymbol{A}_1$ is positive semi-definite if all upper left sub-matrices of $\boldsymbol{A}_1$ have non-negative determinants. This can be written as

$$c_{11}-(\lambda_0 + 2\mu_0) \geqslant 0 \tag{81}$$

$$\begin{vmatrix} c_{11}-(\lambda_0 + 2\mu_0) & c_{12}-\lambda_0 \\ c_{12}-\lambda_0 & c_{22}-(\lambda_0 + 2\mu_0) \end{vmatrix} \geqslant 0 \tag{82}$$

$$\begin{vmatrix} c_{11}-(\lambda_0 + 2\mu_0) & c_{12}-\lambda_0 & c_{13}-\lambda_0 \\ c_{12}-\lambda_0 & c_{22}-(\lambda_0 + 2\mu_0) & c_{23}-\lambda_0 \\ c_{13}-\lambda_0 & c_{23}-\lambda_0 & c_{33}-(\lambda_0 + 2\mu_0) \end{vmatrix} \geqslant 0 \tag{83}$$

The conditions (81)–(83) can be rewritten as

$$\lambda_0 \leqslant c_{11}-2\mu_0 \tag{84}$$

$$a_1\lambda_0 \leqslant b_1 \tag{85}$$

$$a_2\lambda_0 \leqslant b_2 \tag{86}$$

where

$$a_1 = c_{11} + c_{22}-2c_{12}-4\mu_0 \tag{87}$$

$$b_1 = c_{11}c_{22}-c_{12}^2-2(c_{11} + c_{22})\mu_0 + 4\mu_0^2 \tag{88}$$

$$\begin{aligned} a_2 = {} & c_{11}c_{22} + c_{11}c_{33} + c_{22}c_{33}-c_{12}(2c_{33} + c_{12}-c_{13}-c_{23}) \\ & -c_{13}(2c_{22} + c_{13}-c_{12}-c_{23})-c_{23}(2c_{11} + c_{23}-c_{12}-c_{13}) \\ & -4(c_{11} + c_{22} + c_{33}-c_{12}-c_{13}-c_{23})\mu_0 + 12\mu_0^2 \end{aligned} \tag{89}$$

$$\begin{aligned} b_2 = {} & c_{11}c_{22}c_{33} + 2c_{12}c_{13}c_{23}-c_{11}c_{23}^2-c_{22}c_{13}^2-c_{33}c_{12}^2 + 2(-c_{11}c_{22}-c_{11}c_{33}-c_{22}c_{33} \\ & + c_{12}^2 + c_{13}^2 + c_{23}^2)\mu_0 + 4(c_{11} + c_{22} + c_{33})\mu_0^2-8\mu_0^3 \end{aligned} \tag{90}$$

The Lame constants λ_0 and μ_0 are determined so that they are as large as possible while satisfying all conditions (78), (79), (80), (84), (85), (86). The algorithm to compute the equivalent isotropic stiffness matrix can then be written as

1. Compute μ_0 as $\mu_0 = \min\{c_{44}, \ c_{55}, \ c_{66}\}$
2. Compute λ_0 as $\lambda_0 = c_{11}-2\mu_0$
3. Compute a_1, b_1, a_2, and b_2 from Eqs. (87)–(90), respectively. If the computed value for λ_0 in the previous step satisfies the conditions $a_1\lambda_0 \leqslant b_1$ and $a_2\lambda_0 \leqslant b_2$, then exit. Otherwise, reduce λ_0 accordingly.

It should be noted that in the step 3 of the above algorithm, one may adjust both values λ_0 and μ_0 in order to satisfy the conditions $a_1\lambda_0 \leqslant b_1$ and $a_2\lambda_0 \leqslant b_2$. But, since those conditions are first order in terms of λ_0 and higher order in terms of μ_0, we choose to keep μ_0 fixed and determine λ_0 conveniently via linear equations. In this regard, the

condition (71) defined initially is satisfied only in an approximate manner.

7. Numerical results

The problem geometry consists of a transversely isotropic half-space containing a cylindrical hole and in contact with a fluid half-space, while a transducer is placed in the fluid facing the anisotropic half-space. The problem configuration is the same as the one shown in Fig. 1. The length of the modeled half-space in x_1 direction is assumed to be 10 mm. The thicknesses of both the fluid and the solid in x_3 direction are 5 mm. The number of points placed along x_1 direction is 101. This resolution satisfies the convergence criterion that the distance between two adjacent points should be less than the wavelength in the fluid divided by π [1]. Along x_2 direction, 9 points are placed, and the length is chosen such that the distance between two adjacent points is equal in both x_1 and x_2 directions.

The transducer has a circular shape with a radius of 1 mm, and is oriented so that its face is parallel to the fluid-solid interface. The transducer vibrates with a frequency of 1 MHz, and generates time-harmonic waves transmitting through the fluid and hitting the anisotropic solid where it is reflected and refracted at the interface. Due to the high intensity of the generated wave around the transducer, a relatively large resolution is considered in this region and 300 points are used to model the transducer surface.

The fluid is assumed to be water with density $\rho = 1000\,\mathrm{kg/m^3}$ and the P-wave speed $C_p = 1480\,\mathrm{m/s}$. The solid half-space is assumed to have a density of $\rho = 1600\,\mathrm{kg/m^3}$. The stiffness tensor for the solid half-space with x_1 as the axisymmetric direction is assumed to be

$$[\boldsymbol{C}] = \begin{bmatrix} 150 & 18.75 & 18.75 & & & \\ 18.75 & 45 & 21 & & & \\ 18.75 & 21 & 45 & & & \\ & & & 12 & & \\ & & & & 22.5 & \\ & & & & & 22.5 \end{bmatrix} \mathrm{GPa} \tag{91}$$

First, a transversely isotropic half-space with no hole is considered. The axisymmetric direction of the transversely isotropic material is assumed to be aligned with either x_1 or x_2 direction. The distribution of pressure inside the fluid and the stress component σ_{33} inside the solid are considered, and plotted on the central x_1–x_3 plane in Fig. 9. In Fig. 9(a) the axisymmetric direction is x_1 while in Fig. 9(b) this direction is x_2. The wave propagates from fluid into the solid, with the pressure in fluid being equal to the stress component σ_{33} in solid at the interface. One can see that the amount of wave penetration in solid is maximum on the center line ($x_1 = 5$ mm) where the length of wave beam emanating from the transducer is minimum and the wave strikes normal to the interface at this point. As one moves away from this line, the wave amplitude decreases, as is expected. The rate of reduction of reduction of energy penetration is not the same when the fibers run in x_1 direction in Fig. 9(a) and in x_2 direction in Fig. 9(b). This shows that the orientation of the anisotropy has a noticeable effect on the distribution of stress in the solid. The results suggest that the wave tends to stretch more along the fiber direction which is the direction with higher wave velocity.

Next, it is assumed that the axisymmetric direction is the x_1 direction, and the distribution of different stress components are shown in Fig. 10 where the fluid is not plotted to have a clearer view inside the solid. As can be seen, the maximum normal stress σ_{33} is on the central line $x_1 = 0.005$ m while the shear stress σ_{31} is zero on this line due to symmetry. Please note that the distribution and the maximum amplitude of the stress values are different for different stress components. Since the fluid is non-viscous, only the normal component of stress, which is σ_{33} here, is transmitted from the fluid to the solid across the interface. This component shows the highest level of amplitude among all stress components shown in Fig. 10. The other normal components of stress, σ_{11} and σ_{22}, show relatively smaller amplitudes. The shear stress σ_{31} is zero at the interface since the fluid non-viscous. Inside the solid, the shear stress is generated due to non-zero values of normal stress components. The peak value for shear stress is smaller than those of normal stress components.

Then, the axisymmetric direction is assumed to be aligned with the x_2 direction, and the same stress components are plotted in Fig. 11. By comparing Figs. 10 and 11, one can see that the direction of material symmetry has a noticeable effect on the stress field distribution inside the solid. Again, it is observed that the wave tends to stretch more along the fiber direction which exhibits higher wave velocity.

Then, a cylindrical hole of radius $r = 0.5$ mm is considered where the cylinder axis is along x_2 direction. Again, the axisymmetric direction of the transversely isotropic material is assumed to be aligned with either x_1 or x_2 direction, and the same figures as in the case for no hole are plotted. The distribution of pressure inside the fluid and the stress component σ_{33} inside the solid are plotted on central x_1–x_3 plane in Fig. 12. In Fig. 11(a) the material symmetry axis is x_1 while in Fig. 11(b) it is in x_2 direction. As can be seen, the propagation of wave into the solid is interrupted by the hole. The component σ_{33} should be zero on the bottom and top of the hole surface, because of the traction free boundary conditions. This is evident in Fig. 12.

Assuming the symmetry axis oriented in x_1 direction, the distribution of different stress components in solid are shown in Fig. 13. For symmetry axis in x_2 direction, the same stress components are shown in Fig. 14. Comparing these figures with those corresponding to half-space without hole (Figs. 10 and 11) one can see the effect of hole on disturbing the stress field inside the solid. For stress components σ_{33} and σ_{31}, the hole mostly acts as an obstacle on the path of wave propagation, while for the stress components σ_{11} and σ_{22} the blocking of the wave path by the hole is not that obvious.

Lastly, the radius of cylindrical hole is increased from $r = 0.5$ mm to $r = 0.75$ mm, and the same results are plotted. The distribution of pressure inside the fluid and the stress component σ_{33} inside the solid are plotted on central x_1–x_3 plane in Fig. 15. The effect of hole on the wave field is noticeable. The stress pattern generated by the larger and smaller holes in Figs. 12 and 15 are not significantly different.

The distribution of different stress components in solid are shown in Fig. 16 with symmetric axis in x_1 direction, and in Fig. 17 with the symmetric axis in x_2 direction. Comparing these figures with those for the smaller hole (Figs. 13 and 14) one can see the effect of hole size on the distribution of stress field inside the solid.

8. Conclusion

The DPSM technique is extended to ultrasonic wave modeling in an anisotropic half-space containing a hole. The time-harmonic elastodynamic Green's function for anisotropic half-space was evaluated numerically based on the formulation of [47]. For the case of transversely isotropic material, an improved formulation which reduces the integration domain from the hemi-sphere to a quarter-sphere [38] was employed. In addition, a technique called "windowing" previously suggested in [38] was extended here to the case of a half-space with a hole for which only a portion of the domain remains regular. The windowing technique considerably reduces the number of evaluations of Green's function. In order to further reduce the computational cost, a calibration strategy was suggested here to optimize the number of integration points for the regular part of the anisotropic Green's function in terms of the distance between the source and target points. This calibration technique uses an equivalent isotropic stiffness close to the anisotropic one, and results in different resolutions for numerical integration for different distances between source and target points. The developed anisotropic DPSM code was used to simulate ultrasonic wave propagation in a transversely isotropic half-space being in contact with a fluid at its boundary. The results were obtained for different cases. The effect of existence of the holes of different sizes were studied. The

results demonstrate the applicability and effectiveness of the DPSM for modeling ultrasonic wave propagation in an anisotropic medium with an internal anomaly.

Appendix A. Supplementary material

Supplementary data associated with this article can be found, in the online version, at https://doi.org/10.1016/j.ultras.2018.09.002.

References

[1] D. Placko, T. Kundu, DPSM for Modeling Engineering Problems, Wiley, Hoboken, NY, 2007.
[2] T. Kundu, D. Placko, E. Rahani, T. Yanagita, C. Dao, Ultrasonic field modeling: a comparison between analytical, semi-analytical and numerical techniques, IEEE Trans. Ultrason. Ferroelectr. Freq. Control 57 (12) (2010) 2795–2807.
[3] L. Schmerr, Fundamentals of Ultrasonic Nondestructive Evaluation, A Modeling Approach, Springer International Publishing, Switzerland, 2016.
[4] J.A.G. Temple, Modelling the propagation and scattering of elastic waves in inhomogeneous anisotropic media, J. Phys. D: Appl. Phys 21 (1988) 859–874.
[5] Z.Z. Sun, X. Wu, A fully discrete difference scheme for a diffusion-wave system, Appl. Numer. Math. 56 (2) (2006) 193–209.
[6] W.D. Smith, The application of finite element analysis to body wave propagation problems, Geophys. J. Int. 42 (1975) 747–768.
[7] A.V. Pamel, G. Sha, S.I. Rokhlin, M.J.S. Lowe, Finite-element modelling of elastic wave propagation and scattering within heterogeneous media, Proc. Roy. Soc. A. 473 (2017) 20160738.
[8] R. Marklein, The finite integration technique as a general tool to compute acoustic, electromagnetic, elastodynamic, and coupled wave fields, in: Stone WR, editor. Review of radio science 1999–2002, IEEE Press, Piscataway, 2002.
[9] T. Weiland, A discretization method for the solution of maxwells equations for six component fields, Electron. Commun. (AE) 31 (3) (1977) 116–120.
[10] P. Fellinger, A method for the numerical solution of elastic wave propagation problems in the time domain by direct discretization of the elastodynamic governing equations (Ph.D. thesis), University of Kassel, Kassel, Germany, in German, 1991.
[11] P. Fellinger, R. Marklein, K.J. Langenberg, S. Klaholz, Numerical modeling of elastic wave propagation and scattering with efit - elastodynamic finite integration technique, Wave Motion 21 (1995) 47–66.
[12] C.A. Brebbia, J. Domnguez, Boundary Elements: An Introductory Course, second ed., Computation Mechanics Publications, Southampton/McGraw-Hill, New York, 1992.
[13] G.D. Manolis, P.S. Dineva, Elastic waves in continuous and discontinuous geological media by boundary integral equation methods: a review, Soil Dyn. Earthquake Eng. 70 (2015) 11–29.
[14] A.N. Norris, A theory of pulse propagation in anisotropic elastic solids, Wave Motion 9 (1987) 509–532.
[15] M. Spies, Transducer field modeling in anisotropic media by superposition of gaussian base functions, J. Acoust. Soc. Am. 105 (1999) 633–638.
[16] H.L. Lai, R.L. Gibson, K.J. Lee, Quasi-shear wave ray tracing by wavefront construction in 3-d, anisotropic media, J. Appl. Geophys. 69 (2009) 82–95.
[17] P. Delsanto, T. Whitcombe, H. Chaskelis, R. Mignogna, Connection machine simulation of ultrasonic wave propagation in materials: I. The one-dimensional case, Wave Motion 16 (1992) 65–80.
[18] S. Sundararaman, D. Adams, Modeling guided waves for damage identification in isotropic and orthotropic plates using a local interaction simulation approach, J. Vib. Acoust. 130 (2008) 1–16.
[19] Y. Shen, C.E.S. Cesnik, Hybrid local fem/global lisa modeling of damped guided wave propagation in complex composite structures, Smart Mater. Struct. 5 (2016) 1–20.
[20] M. Bouchon, F.J. Sanchez-Sesma, Boundary integral equations and boundary elements methods in elastodynamics, Adv. Geophys. 48 (2007) 157–189.
[21] R.A. Roberts, Ultrasonic beam transmission at the interface between an isotropic and transversely isotropic solid half-space, Ultrasonics 26 (1988) 139–147.
[22] B.P. Newberry, R.B. Thompson, A paraxial theory for the propagation of ultrasonic beams in anisotropic solids, J. Acoust. Soc. Am. 85 (6) (1989) 2290–2300.
[23] O.C. Zienkiewicz, R.L. Taylor, The finite element method, fifth ed., Butterworth-Heinemann, 2000.
[24] P. Kudela, M. Krawczuk, W. Ostachowicz, Wave propagation modelling in 1d structures using spectral finite elements, J. Sound Vib. 300 (2007) 88–100.
[25] P. Kudela, A. Zak, M. Krawczuk, W. Ostachowicz, Modelling of wave propagation in composite plates using the time domain spectral element method, J. Sound Vib. 302 (2007) 728–745.
[26] R. Sridhar, A. Chakraborty, S. Gopalakrishnan, Wave propagation analysis in a anisotropic and inhomogeneous uncracked and cracked structures using pseudospectral finite element method, Int. J. Solids Struct. 43 (16) (2006) 4997–5031.
[27] H. Peng, G. Meng, F. Li, Modeling of wave propagation in plate structures using three-dimensional spectral element method for damage detection, J. Sound Vib. 320 (2009) 942–954.
[28] D. Komatitsch, C. Barnes, J. Tromp, Simulation of anisotropic wave propagation based upon a spectral element method, Geophysics 65 (4) (2000) 1251–1260.
[29] F.H. Quintanilla, M.J.S. Lowe, R.V. Craster, Modeling guided elastic waves in generally anisotropic media using a spectral collocation method, J. Acoust. Soc. Am. 137 (3) (2015).
[30] K. Gaoa, S. Fub, R.L.G. Jr, E.T. Chunge, Y. Efendiev, Generalized multiscale finite-element method (gmsfem) for elastic wave propagation in heterogeneous, anisotropic media, available from: < arXiv:1409.3550v4 > [physics.geo-ph].
[31] Y. Shen, V. Giurgiutiu, Combined analytical fem approach for efficient simulation of lamb wave damage detection, Ultrasonics 69 (2016) 116–128.
[32] D. Placko, N. Liebeaux, Modéle á sources réparties: un concept pour le calcul du champ émis par les circuits magnétiques ouverts, in: Proceedings of 2nd Colloque Interdisciplinaire en Instrumentation (C2I'01) éditions HERMES, CNAM Paris, France, 2001, pp. 523–530.
[33] D. Placko, T. Kundu, Chapter 2: Modeling of Ultrasonic Field by Distributed Point Source Method, in: Ultrasonic Nondestructive Evaluation: Engineering and Biological Material Characterization, CRC Press, 2004.
[34] Y. Wada, T. Kundu, K. Nakamura, Mesh-free distributed point source method for modeling viscous fluid layer motion between disks vibrating at ultrasonic frequency, J. Acoust. Soc. Am. 136 (2) (2014) 466–474.
[35] D. Placko, A. Rivollet, T. Bore, Procédé et dispositif de modélisation d́une grandeur physique d́un écoulement fluide (process and set-up for modeling a physical value in a fluid flow), French Patent (international patent extension pending) Application N 1454675, 23 May 2014.
[36] A.J.C. Jarvis, F.B. Cegla, Scattering of near normal incidence sh waves by sinusoidal and rough surfaces in 3-d: comparison to the scalar wave approximation, IEEE Trans. Ultrason. Ferroelectr. Freq. Control 61 (7) (2014) 1179–1190.
[37] T. Bore, D. Placko, F. Taillade, P. Sabouroux, Electromagnetic characterization of grouting materials of bridge post tensioned ducts for ndt using capacitive probe, NDT & E Int. 60 (2013) 110–120.
[38] S. Fooladi, T. Kundu, Ultrasonic field modeling in anisotropic materials by distributed point source method, Ultrasonics 78 (2017) 115–124.
[39] S. Banerjee, T. Kundu, N. Alnuaimi, Dpsm technique for ultrasonic field modeling near fluid–solid interface, Ultrasonics 46 (2007) 235–250.
[40] S. Banerjee, T. Kundu, Ultrasonic field modeling in plates immersed in fluid, Int. J. Solids Struct. 44 (2007) 6013–6029.
[41] S. Banerjee, T. Kundu, Semi-analytical modeling of ultrasonic fields in solids with internal anomalies immersed in a fluid, Wave Motion 45 (2007) 581–595.
[42] S. Das, S. Banerjee, T. Kundu, Elastic wave scattering in a solid half-space with a circular cylindrical hole using the distributed point source method, Int. J. Solids Struct. 45 (2008) 4498–4508.
[43] A. Shelke, S. Das, T. Kundu, Distributed point source method for modeling scattered ultrasonic fields in the presence of an elliptical cavity, Struct. Health Monitor. 9 (6) (2010) 527–539.
[44] S. Banerjee, T. Kundu, Elastic wave propagation in sinusoidally corrugated waveguides, J. Acoust. Soc. Am. 119 (2006) 2006–2017.
[45] S. Das, C. Dao, S. Banerjee, T. Kundu, Dpsm modeling for studying interaction between bounded ultrasonic beams and corrugated plates with experimental verification, IEEE Trans. Ultrason. Ferroelectr. Freq. Control 54 (2007) 1860–1872.
[46] S. Banerjee, T. Kundu, Elastic wave field computation in multilayered nonplanar solid structures: a mesh-free semi-analytical approach, J. Acoust. Soc. Am. 123 (3) (2008) 1371–1382.
[47] C. Wang, J. Achenbach, Three-dimensional time-harmonic elastodynamic greens functions for anisotropic solids, Proc. Roy. Soc. London A 449 (1995) 441–458.
[48] S. Fooladi, Numerical implementation of elastodynamic greens function for anisotropic media (Master's thesis), University of Arizona, 2016.
[49] M. Sales, L. Gray, Evaluation of the anisotropic greens function and its derivatives, Comput. Struct. 69 (1998) 247–254.
[50] G. Strang, Linear Algebra and its Applications, third ed., Harcourt Brace Jovanovich, Publishers, 1988.